

Computation of High Frequency Magnetoelastic Waves in Layered Materials

Samuel J. Ryskamp and Mark A. Hofer*

Department of Applied Mathematics

University of Colorado Boulder

(Dated: March 2, 2023)

The direct calculation of magnetoelastic wave dispersion in layered media is presented using an efficient, accurate computational technique. The governing, coupled equations for elasticity and magnetism, the Navier and Landau-Lifshitz equations, respectively, are linearized to form a quadratic eigenvalue problem that determines a complex web of wavenumber-frequency dispersion branches and their corresponding mode profiles. Numerical discretization of the eigenvalue problem via a spectral collocation method (SCM) is employed to determine the complete dispersion maps for both a single, finite-thickness magnetic layer and a finite magnetic-nonmagnetic double-layer. The SCM, previously used to study elastic waves in non-magnetic media, is fast, accurate, and adaptable to a variety of sample configurations and geometries. Emphasis is placed on the extremely high frequency regimes being accessed in ultrafast magnetism experiments. The dispersion maps and modes provide insight into how energy propagates through the coupled system, including how energy can be transferred between elastic- and magnetic-dominated waves as well as between different layers. The numerical computations for a single layer are further understood by a simplified analytical calculation in the high-frequency, exchange-dominated regime where the resonance condition required for energy exchange (an anticrossing) between quasi-elastic and quasi-magnetic dispersion branches is determined. Nonresonant interactions are shown to be well approximated by the dispersion of uncoupled elastic and magnetic waves. The methods and results provide fundamental theoretical tools to model and understand current and future magnetic devices powering spintronic innovation.

I. INTRODUCTION

The coupling between a material's vibrational and spin degrees of freedom is a fundamental feature of magnetic materials. While the existence of this coupling has been known for over a century [1–5], most theoretical research has focused on the low frequency regime [6–9] while analytical studies emphasize simple geometries such as the bulk [10, 11] or thin film [9] limits. Many of the magnetic devices that enable current and future spintronic/magnonic applications are multilayer stacks of magnetic and nonmagnetic materials [12–14]. Furthermore, the ultrashort optical or acoustic pulses being used to demagnetize samples in ultrafast magnetism [15, 16] or to approach the plastic limit of a solid in ultrafast magnetoacoustics [17], respectively, are known to excite the extremely high frequency (EHF) band (30–300 GHz) [18–20].

Magnetoelastic coupling [6, 9, 10, 21–23] and layering effects on the dispersion of purely elastic waves [24–27], separately, are active areas of research, but few studies exist that combine them. Although much of the original theoretical work on magnetoelastic coupling is many decades old [10, 28–34], recent technological advances have revived and expanded interest in magnetoelastic waves. At the heart of this growth is the drive to enable energy transfer between phonons and magnons. For example, recent research has studied magnetic spin currents in thin layers, particularly with applications to spintronics and magnonics [12–14]. This interest has led

to experimental advances in the study of magnetoelastic interactions [21–23, 35–37], in part with the goal of generating spin waves by mechanical motion and vice-versa [6, 38]. Other recent applications of magnetoelastic effects include computation [39], logic structures [40], antennas [41], and smart materials [42].

Similarly, there are many physical applications for calculating the dispersion of elastic waves in a layered material, all of which are made more general by the introduction of magnetic coupling. One application is nondestructive evaluation, where elastic waves are excited in a material in order to identify defects or other internal properties [27, 43, 44]. If a material is magnetic, one must take this property into account [45, 46]. Elastic waves in layered materials arise naturally in the geophysical sciences, such as in the propagation of seismic waves [43, 47, 48]. Some have found value by incorporating magnetic effects there as well [49].

Past analytical studies of magnetoelastic waves have primarily focused on either the bulk $d \rightarrow \infty$ or thin film $kd \ll 1$ limits, where k is the angular wavenumber and d is the material thickness [9–11]. These limits admit exact analytical solutions for the dispersion curves, which provide important insight into the nature of phonon-magnon energy conversion. Application of a phenomenological spin wave decomposition has also recently been proposed [50]. The finite thickness regime, where boundary effects must be considered, is more complicated and largely unstudied analytically [6].

A traditional method for determining the dispersion of elastic waves in layered media is the general matrix method (GMM), which involves a complex exponential profile ansatz in the direction of layering [24, 27, 51, 52]. A previous numerical study of magnetoelastic waves uti-

* hofer@colorado.edu

lized a GMM-type approach to trace individual magnetoelastic dispersion curves for surface waves in a magnetic film on a semi-infinite substrate [34]. However, the complexity of the magnetoelastic equations makes the GMM approach impractical for multiple, finite thickness layers. Another, very recent study, utilized post-processing of coupled elastic-micromagnetic, time-dependent simulations to determine the dispersion curves of a single layer magnetoelastic wave guide by extracting space-time frequency curves for certain configurations of initial, boundary data [9]. Both of these approaches are quite computationally intensive. To our knowledge, the full dispersion map of a magnetoelastic, layered material has never been determined directly.

Despite the typical layered geometry of magnetic devices and the high frequencies now being accessed, there are few developed theoretical tools for investigating magnetoelastic wave propagation and little in the way of comprehensive descriptions for these common configurations and operating regimes. In this paper, we directly compute wavenumber-frequency dispersion maps and the corresponding vertical mode profiles of magnetoelastic, layered materials using the spectral collocation method (SCM), an accurate, fast numerical method to compute dispersion maps and mode profiles for single and multiple, finite thickness magnetic and elastic layers. A recent innovation for calculating elastic dispersion in nonmagnetic materials, the SCM utilizes a discretization at special points (zeros of Chebyshev polynomials) and differentiation matrices for derivatives in the direction perpendicular to the layering in order to achieve efficient, accurate computation [25, 26, 53]. The linearized magnetoelastic equations result in a quadratic eigenvalue problem. For a fixed wavenumber, each eigenvalue corresponds to a frequency branch and the corresponding eigenvector is an interpolant for the vertical mode profiles of magnetic and elastic components in each layer. The mode profiles are used to classify dispersion branches in terms of the energy residing in elastic or magnetic components and in which layer the energy is concentrated. Using the SCM, we calculate and analyze full magnetoelastic dispersion maps for a yttrium-iron-garnet (YIG) single layer, YIG on a nonmagnetic gadolinium gallium garnet (GGG) substrate, and nickel (Ni) on a nonmagnetic silicon nitride (Si_3N_4) substrate. This method is shown to be easy to implement and is rapidly convergent, with computational times measured in minutes on a conventional laptop computer.

For magnetoelastic boundary value problems, other discretization methods such as traditional finite differences applied to N equispaced grid points, exhibit errors that decrease algebraically $\mathcal{O}(N^{-n})$ for some n . Usually, $n = 2$ is used in practice. The SCM method benefits from its superior accuracy because interpolation at the nonuniform Chebyshev points is almost optimal in a certain sense, achieving errors that decrease faster than any power of N for smooth functions [54, 55]. We observe almost exponential convergence $\mathcal{O}(e^{-N})$ in our compu-

tations (see the validation study in App. B), hence many fewer grid points are required to obtain accurate results with the SCM method than for traditional finite differences, providing significant computational speedup. About $N = 12$ grid points per layer is sufficient for the regimes studied here to achieve high resolution. Furthermore, the clustering of Chebyshev grid points near interfaces ensures high resolution of surface modes and other interfacial mode features.

Our numerical computations are complemented by an analytical calculation in the EHF, exchange-dominated regime that is used to explicitly determine magnetoelastic dispersion curves in a single, finite thickness ferromagnetic layer. We find that crossings between phonon and magnon dispersion branches can be resonant or nonresonant in the presence of magnetoelastic coupling. If the vertical mode profiles are of the same order, they are resonant and an anticrossing appears. Anticrossings result in the transfer of energy between quasi-elastic and quasi-magnetic dispersion branches with a well-defined gap width linearly proportional to the magnetoelastic coupling. If the waves are nonresonant, no anticrossing occurs, and the dispersion branches intersect with very weak modification that is proportional to the square of the magnetoelastic coupling. Our calculations also show that the magnetoelastic gap width decreases with increasing frequency and decreasing wave number.

Our work is also motivated by recent experiments where an ultrafast X-ray free electron laser (XFEL) was used to excite and measure far-from-equilibrium conditions in layered magnetic samples [20, 56, 57]. Because of this, we focus primarily on EHF, exchange-dominated interactions with a perpendicular applied field. However, these choices are incidental to the applicability of the SCM approach. The SCM is quite general and can be readily applied to similar problems involving in-plane fields, lower frequencies, more complex anisotropies, and even non-planar geometries. We will demonstrate some of this versatility by presenting dispersion curves for multiple materials and sample sizes in the EHF band as well as in the more traditional single GHz regime.

The outline of this work is as follows. After introducing the Navier and Landau-Lifshitz equations for elasticity and magnetism in Sec. II, their linearization about a perpendicularly magnetized, static configuration in Sec. III results in a quadratic eigenvalue problem in differential form. An asymptotic analysis of this eigenvalue problem, neglecting dipole effects, for weak magnetoelastic coupling in Sec. IV determines the resonance condition for anticrossings and phonon-magnon energy transfer. In Sec. V, we introduce the spectral collocation method (SCM) and use it in Sec. VI to compute dispersion maps for single and double layer films of various thicknesses. Finally, we conclude with a discussion in Sec. VII.

II. GOVERNING EQUATIONS

This section summarizes the equations for magnetoelastic waves mostly following [9, 58], with additional material synthesized from other references including [10, 11]. Additional helpful sources regarding magnetic and elastic waves include [28, 30, 34, 59–62].

A. Energy density

The energy density of a magnetoelastic material consists of the following components [9]

$$\mathcal{E}_{\text{tot}} = \mathcal{E}_{\text{dip}} + \mathcal{E}_{\text{ex}} + \mathcal{E}_Z + \mathcal{E}_{\text{an}} + \mathcal{E}_{\text{el}} + \mathcal{E}_{\text{kin}} + \mathcal{E}_c. \quad (1)$$

These terms represent, from left to right, the energy density due to dipole (demagnetization) effects, exchange interactions, the Zeeman effect (applied field), anisotropy energy, elastic potential, kinetic energy, and magnetoelastic coupling. For a material with magnetization vector \mathbf{M} , the first three energy density quantities are calculated as

$$\mathcal{E}_{\text{dip}} = -\frac{\mu_0}{2}(\mathbf{M} \cdot \mathbf{H}_{\text{dip}}), \quad (2)$$

$$\mathcal{E}_{\text{ex}} = \frac{A_{\text{ex}}}{M_s} |\nabla \mathbf{M}|^2, \quad (3)$$

$$\mathcal{E}_Z = -\mu_0(\mathbf{M} \cdot \mathbf{H}_0). \quad (4)$$

where A_{ex} is the exchange stiffness coefficient, M_s is the saturation magnetization of the material, $\mu_0 = 4\pi \times 10^{-7}$ H/m is the magnetic permeability of free space, \mathbf{H}_{dip} is the induced field by the magnet, which is computed here under the magnetostatic approximation of Maxwell's equations by assuming that wave speeds are much smaller than the speed of light (see eq. (11)), and \mathbf{H}_0 is an applied external field. The intrinsic crystalline anisotropy energy density \mathcal{E}_{an} depends on the material's favored direction of magnetization. For a magnetically cubic material, this is calculated as [59]

$$\mathcal{E}_{\text{an}} = \frac{K_1}{M_s^2} \sum_{i \neq j} M_i^2 M_j^2 + \frac{K_2}{M_s} M_1^2 M_2^2 M_3^2.$$

In the materials of interest here, the intrinsic crystalline anisotropy is weaker than the other energy terms [21, 63]. In the interest of simplicity, we will ignore it but its incorporation into the computation of magnetoelastic dispersion is straightforward because it is a local, undifferentiated effective field term.

Under Hooke's Law, which assumes a linear relationship between stress and strain, the elastic energy density is calculated as [10, 64]

$$\mathcal{E}_{\text{el}} = \frac{1}{2} \sum_{i,j} \sigma_{ij} \varepsilon_{ij}, \quad (5)$$

where σ is the stress tensor and ε is the strain tensor. Kinetic energy for the displacement \mathbf{u} is calculated as

$$\mathcal{E}_{\text{kin}} = \frac{\rho}{2} |\mathbf{u}_t|^2, \quad (6)$$

where ρ is the material density.

The coupling energy for a cubic material is calculated as an expansion of anisotropy and elastic energy around the strain ε and the magnetization \mathbf{M} as [10]

$$\begin{aligned} \mathcal{E}_c = & \frac{B_1}{M_s^2} (\varepsilon_{11} M_1^2 + \varepsilon_{22} M_2^2 + \varepsilon_{33} M_3^2) + \\ & + \frac{2B_2}{M_s^2} (\varepsilon_{12} M_1 M_2 + \varepsilon_{23} M_2 M_3 + \varepsilon_{31} M_1 M_3). \end{aligned} \quad (7)$$

The coupling coefficients in an isotropic medium are defined as $B_1 = -3\mu\lambda_{100}$ and $B_2 = -3\mu\lambda_{111}$, where μ is the Lamé coefficient and λ_{100} and λ_{111} are dimensionless coupling coefficients for a particular material.

The total energy in the magnetic material occupying the region U is calculated by a volume integral of the energy density,

$$E = \int_U \mathcal{E}_{\text{tot}} d\mathbf{x}. \quad (8)$$

Equilibrium states of a magnetoelastic material are local minima of the total energy E (8).

B. Magnetism

The relaxation from a non-equilibrium state of the magnetization vector $\mathbf{M}(\mathbf{x}, t)$, defined within the region $U \subset \mathbb{R}^3$ is governed by the Landau-Lifshitz-Gilbert equation [60, 65, 66],

$$\begin{aligned} \frac{\partial \mathbf{M}}{\partial t} = & -|\gamma| \mu_0 \mathbf{M} \times \mathbf{H}_{\text{eff}} + \frac{\alpha}{M_s} \mathbf{M} \times \frac{\partial \mathbf{M}}{\partial t}, \\ \mathbf{H}_{\text{eff}} = & -\frac{1}{\mu_0} \frac{\delta E}{\delta \mathbf{M}}. \end{aligned} \quad (9)$$

where α is the nondimensional Gilbert damping parameter and $|\gamma| = 1.76 \times 10^{-11}$ rad/Ts is the gyromagnetic ratio for an electron. One important property of (9) is that the magnitude of \mathbf{M} is conserved, and this magnitude is called the saturation magnetization M_s of the material, i.e. $|\mathbf{M}| = M_s$. Consequently, it is often convenient to refer to the normalized vector field $\boldsymbol{\zeta} = \mathbf{M}/M_s$ so that $|\boldsymbol{\zeta}| = 1$.

The effective magnetic field \mathbf{H}_{eff} is calculated as the variational derivative of the total energy (8) with respect to magnetization [67]. Since there are five components of the energy (1) that depend on \mathbf{M} , the effective magnetic field can be decomposed into five corresponding components,

$$\mathbf{H}_{\text{eff}} = \mathbf{H}_{\text{dip}} + \mathbf{H}_{\text{ex}} + \mathbf{H}_0 + \mathbf{H}_{\text{an}} + \mathbf{H}_c. \quad (10)$$

The dipole field \mathbf{H}_{dip} , also known as the stray field or the demagnetizing field, is obtained by solving Maxwell's equations [67–69], in which the magnetization induces a magnetic field. We will assume the magnetostatic approximation, which ignores the time variation of electric fields, reducing Maxwell's equations to

$$\nabla \cdot \mathbf{B} = 0, \quad (11a)$$

$$\nabla \times \mathbf{H}_{\text{dip}} = 0, \quad (11b)$$

where \mathbf{B} is the total magnetic induction field

$$\mathbf{B} = \mu_0(\mathbf{H}_{\text{dip}} + \mathbf{M}). \quad (11c)$$

The appropriate boundary conditions are [69]

$$\mathbf{B} \cdot \mathbf{n} = \text{continuous}, \quad \mathbf{x} \in \partial U, \quad (11d)$$

$$\mathbf{H}_{\text{dip}} \times \mathbf{n} = \text{continuous}, \quad \mathbf{x} \in \partial U, \quad (11e)$$

$$\lim_{|\mathbf{x}| \rightarrow \infty} \mathbf{H}_{\text{dip}} = 0, \quad \mathbf{x} \in U^C \setminus \partial U, \quad (11f)$$

where ∂U is the boundary of U . The exchange field is due to the property that ferromagnetic materials tend to align spins along a common direction [67] and is given by

$$\mathbf{H}_{\text{ex}} = \ell^2 \Delta \mathbf{M}, \quad (12)$$

where ℓ is the exchange length of the material defined as $\ell^2 = 2A_{\text{ex}}/(\mu_0 M_s^2)$. Physically, ℓ represents the length scale where exchange effects are dominant. For lengths much larger than ℓ , dipole effects dominate.

Although the materials considered here are magnetically cubic, we will assume that the effect of this anisotropy on the total effective field is small enough so that it can be ignored. Finally, the effective field due to magnetoelastic coupling can be calculated from the coupling energy density (7) as

$$\mathbf{H}_c = -\frac{2}{\mu_0 M_s} \begin{bmatrix} B_1 \varepsilon_{11} \zeta_1 + B_2 (\varepsilon_{12} \zeta_2 + \varepsilon_{13} \zeta_3) \\ B_1 \varepsilon_{22} \zeta_2 + B_2 (\varepsilon_{12} \zeta_1 + \varepsilon_{23} \zeta_3) \\ B_1 \varepsilon_{33} \zeta_3 + B_2 (\varepsilon_{13} \zeta_1 + \varepsilon_{23} \zeta_2) \end{bmatrix}. \quad (13)$$

The boundary conditions for magnetism are free spin, i.e.

$$\nabla_{\mathbf{n}} \cdot \mathbf{M} = 0, \quad \mathbf{x} \in \partial U, \quad (14)$$

where \mathbf{n} is the unit vector normal to the surface, and $\nabla_{\mathbf{n}} \cdot \mathbf{M}$ represents the divergence in the direction of \mathbf{n} .

Recently, inertial effects have been observed in magnetic samples driven at 0.4–1.0 THz frequencies [70]. Inertia drives spin nutation corresponding to the relaxation of angular momentum. Inertia can be modeled by the addition of a second derivative in time term proportional to $\alpha\tau/T$ to the Landau-Lifshitz-Gilbert equation (9) [71, 72]. Here, τ is the material-dependent angular momentum relaxation time—estimated and recently measured for NiFe and CoFeB [70], to be in the 1–100 ps range—and T is the precessional timescale—about 10 ps—1 ns here. Inertial effects may be relevant when the effective field contribution, scaling with the nondimensional

parameter $\alpha\tau/T$, is comparable to other effective field terms of interest. For the materials in the present study, we estimate $\alpha\tau/T$ to be no larger than 10^{-3} (and much smaller in many cases) whereas the nondimensional magnetoelastic coupling strength is $\epsilon \approx 0.02$ (see eq. (41)). Since the EHF regime studied here is below the THz frequency range and magnetoelastic coupling is sufficiently strong in the materials studied, we neglect inertia [72].

C. Elasticity

The elastic displacement \mathbf{u} in the linear regime is governed by the equation

$$\rho \mathbf{u}_{tt} = \mathbf{f}, \quad \mathbf{f} = \nabla \cdot \boldsymbol{\sigma} = \nabla \cdot \frac{\delta E}{\delta \boldsymbol{\varepsilon}}. \quad (15)$$

With constant temperature, the variational derivative of energy is the stress tensor $\frac{\delta E}{\delta \boldsymbol{\varepsilon}} = \boldsymbol{\sigma}$. We assume an isotropic elastic material and neglect acoustic damping. Then, Hooke's law for the total stress $\boldsymbol{\sigma}$ in terms of the strain $\boldsymbol{\varepsilon}$ depends on two parameters,

$$\boldsymbol{\sigma} = \lambda \text{tr}(\boldsymbol{\varepsilon}) \mathbf{I} + 2\mu \boldsymbol{\varepsilon}.$$

The constants λ and μ are the Lamé moduli with units of stress. For small displacements, we can in general approximate the total strain tensor $\boldsymbol{\varepsilon}$ as

$$\varepsilon_{ij} = (\partial_j u_i + \partial_i u_j)/2.$$

Combining the above equations, we obtain a forced Navier equation for homogeneous, linear, isotropic magnetoelastic deformations

$$(\lambda + 2\mu) \nabla(\nabla \cdot \mathbf{u}) - \mu \nabla \times \nabla \times \mathbf{u} + \mathbf{f}(\mathbf{m}) = \rho \ddot{\mathbf{u}}, \quad (16)$$

where \mathbf{f} arises from the magnetoelastic coupling energy E_c . When $\mathbf{f} \equiv \mathbf{0}$ (i.e. with no magnetic effects present), by a Helmholtz decomposition we can recover the two bulk speeds of sound for an isotropic material [61], the shear speed c_S and the longitudinal speed c_L

$$c_S = \sqrt{\mu/\rho}, \quad c_L = \sqrt{(\lambda + 2\mu)/\rho}, \quad (17)$$

subject to the ordering $c_S < c_L$. The variational derivative of the coupling energy E_c yields the magnetic component of the stress $\frac{\delta E_c}{\delta \boldsymbol{\varepsilon}} = \boldsymbol{\sigma}^c$. The divergence of the magnetic stress $\mathbf{f} = \nabla \cdot \boldsymbol{\sigma}^c$ is the forcing term in the Navier equation,

$$\mathbf{f} = 2B_1 \begin{bmatrix} \zeta_1 \frac{\partial \zeta_1}{\partial x_1} \\ \zeta_2 \frac{\partial \zeta_2}{\partial x_2} \\ \zeta_3 \frac{\partial \zeta_3}{\partial x_3} \end{bmatrix} + B_2 \begin{bmatrix} \zeta_1 \left(\frac{\partial \zeta_2}{\partial x_2} + \frac{\partial \zeta_3}{\partial x_3} \right) + \zeta_2 \frac{\partial \zeta_1}{\partial x_2} + \zeta_3 \frac{\partial \zeta_1}{\partial x_3} \\ \zeta_2 \left(\frac{\partial \zeta_1}{\partial x_1} + \frac{\partial \zeta_3}{\partial x_3} \right) + \zeta_1 \frac{\partial \zeta_2}{\partial x_1} + \zeta_3 \frac{\partial \zeta_2}{\partial x_3} \\ \zeta_3 \left(\frac{\partial \zeta_1}{\partial x_1} + \frac{\partial \zeta_2}{\partial x_2} \right) + \zeta_1 \frac{\partial \zeta_3}{\partial x_1} + \zeta_2 \frac{\partial \zeta_3}{\partial x_2} \end{bmatrix}. \quad (18)$$

For an elastic material, the boundary conditions at the surface are

$$\mathbf{f}_{\text{surf}} = \boldsymbol{\sigma} \mathbf{n}, \quad \mathbf{x} \in \partial U. \quad (19)$$

where \mathbf{f}_{surf} is the traction force per unit surface (or stress) at the boundary.

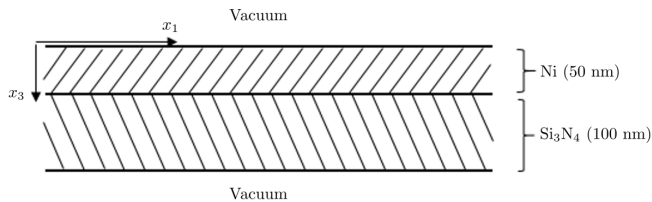


FIG. 1. The experimental medium for which we are calculating the magnetoelastic dispersion relation: 100 nm of silicon nitride (Si_3N_4), a nonmagnetic substrate, supporting 50 nm of nickel, surrounded by a vacuum. For modeling purposes, the material is considered to be infinite in the x_1 and x_2 directions.

III. LINEARIZED MAGNETOELASTIC EQUATIONS

A. Physical assumptions

We consider two magnetic and nonmagnetic materials. They are chosen for their use in recent experiments, their low magnetic damping in the case of YIG, and their relatively large magnetoelastic coupling. One of the double layers we study consists of 100 nm of Si_3N_4 supporting a 50 nm layer of nickel. See Fig. 1 for a schematic. Besides this material sample, we will also study a 30 nm single layer of YIG and both 30 nm/50 nm, 200 nm/300 nm YIG/GGG double layers. YIG has been classically studied in the context of magnetoelastic interactions due to its very low magnetic damping (cf. [11, 34]), and GGG is a natural substrate for YIG [34]. YIG and GGG have the added advantage of comparable shear speeds of sound, which will simplify the visualization of their dispersion relations. The material parameters are shown in Table I.

	Ni [73]	Si_2N_3 [74]	YIG [11, 63]	GGG [75]
c_L (m/s)	6040	8000	7200	6400
c_S (m/s)	3000	4500	3800	3500
ρ (kg/m^3)	8900	3250	5170	7080
B_1 (MJ/m^3)	9.38 [76]	X	3.5	X
B_2 (MJ/m^3)	10 [76]	X	7	X
ℓ (nm)	7.72 [77]	X	17.3	X
M_s (kA/m)	480 [77]	X	140	X

TABLE I. Parameter values for the four materials studied in this paper. The parameter values for Si_2N_3 were chosen from the ranges given by [74] in order to minimize the shear speed, allowing for easier visualization.

In this paper, we assume that all materials are elastically isotropic, and that the magnetic lattice is cubic. We also assume that the material is infinitely wide in the transverse x_1 and x_2 directions, the displacements are small and therefore linear, and the waves of interest propagate in the x_1 -direction. We will limit ourselves to materials with either a single magnetic layer, or a single magnetic layer on a nonmagnetic substrate, with

the magnetic layer in both cases vertically localized to $0 < x_3 < d$.

The nondimensional Gilbert damping parameter α is as low as 3×10^{-5} for YIG [78]. Nickel is a metallic ferromagnet where α was measured to be 0.024 [79]. The nondimensional magnetoelastic coupling strength is estimated to be $\epsilon \approx 0.02$ for YIG and Ni (see eq. (41)) so is much stronger than damping in YIG. Our focus here is on the real frequency response due to magnetoelastic coupling of layered devices in the EHF regime, hence we will neglect magnetic damping for our analysis, which is a reasonable physical assumption for YIG and transition metal alloys. Therefore, all but one presented computational example is for YIG. We compute the magnetoelastic dispersion of Ni/SiN while neglecting damping, even though its strength is comparable to magnetoelastic coupling, in order to convey the robustness of the SCM method to material properties. Damping introduces a nonzero imaginary part to the frequency corresponding to wave attenuation and a nonzero frequency linewidth [34]. Large enough damping could smear out the resonant frequency anticrossings predicted here.

We assume that a magnetic field \mathbf{H}_0 is applied in the x_3 -direction, perpendicular to the plane of the material, so that $\mathbf{H}_0 = [0 \ 0 \ H_0]^T$. The magnetic field is sufficiently strong that, in the absence of waves, the magnetization is saturated in the x_3 -direction. This occurs when $H_0 \geq M_s$. In order to ensure saturation magnetization in the vertical direction, we choose $\mu_0 H_0 = 0.25$ T for the calculations involving YIG, and $\mu_0 H_0 = 0.65$ T for the calculations involving nickel.

It is important to stress that nearly all of these assumptions can be relaxed without reducing the effectiveness of the SCM approach, which is very versatile. SCM can be readily generalized to situations with other geometries, more complex elastic or magnetic anisotropies [25], and to other physical effects such as magnetic/acoustic damping and spin inertia. What we focus on here is a minimal but realistic model of the physics of layering and magnetoelastic coupling in the ultrafast regime.

B. Elastic equations

We look for linear wave solutions of the form

$$\mathbf{u}(\mathbf{x}, t) = \begin{bmatrix} A_1(x_3) \\ A_2(x_3) \\ A_3(x_3) \end{bmatrix} e^{i(kx_1 - \omega t)}. \quad (20)$$

Inserting (20) into (16) and dividing out the common exponential factor yields, after substituting in the speeds

(17),

$$-\omega^2 A_1 = -c_L^2 k^2 A_1 + c_S^2 A_1'' + (c_L^2 - c_S^2) i k A_3' + \frac{f_1}{\rho}, \quad (21a)$$

$$-\omega^2 A_2 = c_S^2 (A_2'' - k^2 A_2) + \frac{f_2}{\rho}, \quad (21b)$$

$$-\omega^2 A_3 = c_L^2 A_3'' - c_S^2 k^2 A_3'' + (c_L^2 - c_S^2) i k A_1' + \frac{f_3}{\rho}, \quad (21c)$$

where a prime denotes differentiation with respect to x_3 . Here, f_i/ρ should also be understood to be divided by the common exponential factor.

C. Magnetic equations

For small oscillations, we linearize the magnetic waves around the vertical saturation magnetization as

$$\begin{aligned} \mathbf{M}(\mathbf{x}, t) &= \mathbf{M}_0 + \mathbf{m}(\mathbf{x}, t), \\ &= \begin{bmatrix} 0 \\ 0 \\ M_s \end{bmatrix} + \begin{bmatrix} m_1(x_3) \\ m_2(x_3) \\ 0 \end{bmatrix} e^{i(kx_1 - \omega t)}, \end{aligned} \quad (22)$$

where $m_1, m_2 \ll M_s$. Since we are only interested in real dispersion relations for ω and k , we will neglect the damping in (9) to obtain an undamped Landau-Lifshitz equation, also known as the Larmor torque equation,

$$\frac{\partial \mathbf{M}}{\partial t} = -\gamma \mu_0 \mathbf{M} \times \mathbf{H}_{\text{eff}}. \quad (23)$$

Given the linearization (22), the exchange field (12) has the form $\mathbf{H}_{\text{ex}} = \ell^2 (\mathbf{m}'' - k^2 \mathbf{m})$.

In order to determine the field due to dipole effects \mathbf{H}_{dip} we must first solve the magnetostatic Maxwell equations (11). Since the dipole field is curl free, it is the gradient of a scalar

$$\mathbf{H}_{\text{dip}} = \begin{cases} -\nabla \phi^+, & d < x_3, \\ -\nabla \phi, & 0 < x_3 < d, \\ -\nabla \phi^-, & x_3 < 0. \end{cases} \quad (24)$$

We follow [69] to obtain a simplified equation for the dipole field. In the absence of waves, $\mathbf{M} = \mathbf{M}_0$ in (22) and the dipole field (24) with $\phi = \phi_0$ satisfying (11) is

$$\phi_0 = M_s x_3, \quad \phi_0^+ = M_s d, \quad \phi_0^- = 0. \quad (25)$$

For the wave-only term $\mathbf{M} = \mathbf{m}$ in (22), we seek a solution of (11) in the form

$$\varphi = g(x_3) e^{i(kx_1 - \omega t)}, \quad \varphi^\pm = g^\pm(x_3) e^{i(kx_1 - \omega t)} \quad (26)$$

for the dipole field (24) with $\phi = \varphi$. Then, eq. (11a) with (11c) imply

$$-k^2 g(x_3) + g''(x_3) = i k m_1(x_3), \quad (27a)$$

$$-k^2 g^\pm(x_3) + (g^\pm)''(x_3) = 0. \quad (27b)$$

Equation (27b) with the boundary condition (11f) is solved with $g^\pm(x_3) = C_\pm e^{\mp k x_3}$. Since the second component of \mathbf{H}_{dip} is zero (no x_2 dependence in (24)), we can impose (11e) by taking $g(d) = C_+ e^{-kd}$, $g(0) = C_-$. The boundary condition (11d) implies $g'(d) = -k C_+ e^{-kd}$, $g'(0) = k C_-$. Eliminating C_\pm by combining these two conditions we obtain

$$\begin{aligned} -k^2 g(x_3) + g''(x_3) &= i k m_1(x_3), \\ g'(d) = -k g(d), \quad g'(0) &= k g(0), \end{aligned} \quad (28)$$

so that the complete dipole potential is $\phi = \phi_0 + \varphi$ and the corresponding dipole field inside the magnet is

$$\mathbf{H}_{\text{dip}} = -\nabla \phi = \begin{bmatrix} -i k g(x_3) e^{i(kx_1 - \omega t)} \\ 0 \\ -g'(x_3) e^{i(kx_1 - \omega t)} - M_s \end{bmatrix}, \quad (29)$$

Note that no averaging assumptions were made for the dipole field (29), which is an exact solution to the magnetostatic Maxwell equations (11). Although eq. (28) can be solved using Green's function techniques [80], we will obtain it numerically as part of the SCM.

D. Coupling

From the magnetic wave ansatz (22) we can approximate $\zeta_3 \approx 1$, $\zeta_2 \approx \zeta_1 \approx 0$, $\partial \zeta_3 / \partial x_i \approx 0$. The magnetoelectric forcing terms from (18) simplify to

$$\mathbf{f} = \frac{B_2}{M_s} \begin{bmatrix} m_1' \\ m_2' \\ i k m_1 \end{bmatrix} e^{i(kx_1 - \omega t)}. \quad (30)$$

The effective field due to elastic coupling from (23) and (10) also simplifies to become

$$\mathbf{H}_c = -\frac{1}{\mu_0 M_s} \begin{bmatrix} B_2 (A_1' + i k A_3) \\ B_2 A_2' \\ 2 B_1 A_3' \end{bmatrix} e^{i(kx_1 - \omega t)}. \quad (31)$$

Inserting (30) into (21) and (10) into (23) and neglecting quadratic terms yields

$$-\omega^2 A_1 = -c_L^2 k^2 A_1 + c_S^2 A_1'' + (c_L^2 - c_S^2) i k A_3' + \frac{B_2 m_1'}{\rho M_s}, \quad (32a)$$

$$-\omega^2 A_2 = c_S^2 (A_2'' - k^2 A_2) + \frac{B_2 m_2'}{\rho M_s}, \quad (32b)$$

$$-\omega^2 A_3 = c_L^2 A_3'' - c_S^2 k^2 A_3 + (c_L^2 - c_S^2) i k A_1' + \frac{i k B_2 m_1}{\rho M_s}, \quad (32c)$$

$$i \omega m_1 = \gamma \mu_0 \left[(H_0 - M_s + \ell^2 M_s k^2) m_2 - \ell^2 M_s m_2'' + \frac{B_2 A_2'}{\mu_0} \right], \quad (32d)$$

$$i \omega m_2 = \gamma \mu_0 \left[(-H_0 + M_s - \ell^2 M_s k^2) m_1 + \ell^2 M_s m_1'' - i k M_s g - \frac{B_2 A_1'}{\mu_0} + \frac{i k B_2 A_3}{\mu_0} \right], \quad (32e)$$

where g satisfies (28). Equations (32) and (28) are a system of six ordinary differential equations for six variables in a magnetoelastic layer. Note that the first coupling coefficient B_1 plays no role in the linearized system. For a purely elastic layer, $B_2 = 0$, and the system reduces to the three elastic equations.

E. Boundary conditions

We must also incorporate boundary conditions to close the above system. For a purely elastic layer, we have three second-order equations, requiring six boundary conditions. These come from continuity of the three stresses σ_{j3} (19) and three displacements A_j , $j \in \{1, 2, 3\}$ at a boundary. If the boundary is with vacuum, we instead require that $\sigma_{j3} = 0$ at those boundaries. The magnetoelastic stresses are calculated as $\sigma = \delta(E_c + E_{el})/\delta\varepsilon$, yielding

$$\sigma_{13} = \mu(A_1' + i k A_3) + \frac{B_2}{M_s} m_1, \quad (33a)$$

$$\sigma_{23} = \mu A_2' + \frac{B_2}{M_s} m_2, \quad (33b)$$

$$\sigma_{33} = \lambda i k A_1 + (\lambda + 2\mu) A_3'. \quad (33c)$$

For a magnetic layer, we include the Neumann conditions for magnetization elements (14) $\partial m_j / \partial x_3 = 0$, $j \in \{1, 2\}$, along with the Robin conditions for the dipole field (28).

Since eigenfunctions are multiplied by a complex exponential, the mode profile is the real part of $[A_1 \ A_2 \ A_3 \ m_1 \ m_2] e^{i(kx_1 - \omega t)}$. Based on the symmetry properties of equations (32) and the associated boundary conditions, eigenfunctions can be normalized so that

$$\text{Re} \begin{bmatrix} A_1 \\ m_1 \end{bmatrix} = 0 \quad \text{and} \quad \text{Im} \begin{bmatrix} A_2 \\ A_3 \\ m_2 \end{bmatrix} = 0. \quad (34)$$

Consequently, modes oscillate between populating the longitudinal components A_1 , m_1 and then the transverse components A_2 , A_3 , and m_2 , which are $\pi/2$ out of phase.

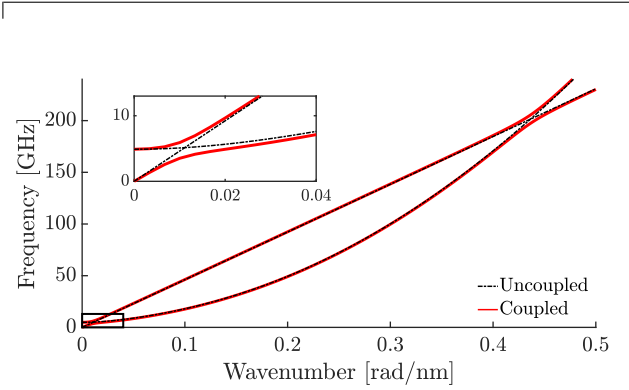


FIG. 2. Coupled (solid) and uncoupled (dashed-dotted) dispersion curves for bulk nickel with an applied field perpendicular to the direction of wave propagation. The uncoupled curves have two interactions, where for coupled curves anticrossings appear. The lower-frequency anticrossing is shown zoomed-in in the inset. The applied field has magnitude $\mu_0 H_0 = 0.65$ T. The coupling coefficient B_2 here is chosen to be unphysically large ($B_2 = 20$ MJ/m³) in order to visually emphasize anticrossing behavior; all other material constants are as in Table I.

Due to the property (34), taking the imaginary part of the boundary condition (33a) implies that A_1' can be discontinuous across the interface between a magnet and non-magnet.

IV. ANALYTICAL CALCULATIONS

A. Bulk magnetoelastic waves

The dispersion relations for magnetoelastic waves in a bulk material with $d \rightarrow \infty$ can be calculated directly from (32). In this case, all derivatives with respect to x_3 are assumed to be negligibly small, and boundary effects are ignored. The resulting sixth-order homogeneous linear system for A_i , m_j , and g requires a nonzero determinant in order for there to be a nonzero solution. This relation then yields a sextic polynomial equation for ω .

First, we consider uncoupled waves ($B_2 = 0$). For the

three purely elastic waves, the dispersion then is

$$\omega_{\text{el}} = ck, \quad (35)$$

where c is one of the speeds of sound (17). For A_1 , the wave is longitudinal and travels with speed c_L , while for A_2 and A_3 the wave is transverse (shear) and travels with speed c_S . The dispersion for magnetic waves in a bulk material with a perpendicular applied field is

$$\omega_{\text{m}} = \pm [(\omega_{\text{H}} - \omega_{\text{M}} + \beta k^2)(\omega_{\text{H}} + \beta k^2)]^{1/2}, \quad (36)$$

where

$$\omega_{\text{H}} = \gamma\mu_0 H_0, \quad \omega_{\text{M}} = \gamma\mu_0 M_{\text{s}}, \quad \beta = \gamma\mu_0 \ell^2 M_{\text{s}}. \quad (37)$$

Note that (36) differs slightly from what is typically presented (cf. [11]), since the $d \rightarrow \infty$ limit of our equations (32) retains a $-M_{\text{s}}$ term due to the demagnetizing effect of the material boundaries.

Next, we consider the dispersion of (32) with nonzero magnetoelastic coupling ($B_2 \neq 0$). In the bulk limit, A_1 and A_2 separate from the magnetic terms and the corresponding waves travel with the uncoupled speeds c_L and c_S , respectively. The remaining elastic component A_3 and the magnetic components m_1 and m_2 form coupled magnetoelastic waves subject to the quartic dispersion relation

$$(\omega^2 - \omega_{\text{m}}^2)(\omega^2 - \omega_{\text{el}}^2) - \frac{\gamma B_2^2}{\rho M_{\text{s}}} (\omega_{\text{H}} - \omega_{\text{M}} + \beta k^2) k^2 = 0, \quad (38)$$

where $\omega_{\text{el}} = c_S k$. In Fig. 2, we show the positive, uncoupled and coupled magnetoelastic dispersion curves for A_3 and magnetism in a bulk material subject to a perpendicular applied field.

The coupled and uncoupled bulk dispersion curves present some general principles regarding magnetoelastic wave interactions. As evident from Fig. 2, magnetoelastic interactions are most significant near the intersections of the uncoupled magnetic and elastic dispersion curves where anticrossings appear. Instead of intersecting, the dispersion curves bend away from one another, leaving a gap. The gap width between the curves is determined by the strength of the magnetoelastic coupling B_2 [9, 11]. Far away from the anticrossing, the dispersion curves follow the uncoupled magnetic or elastic curves and are known as quasi-magnetic and quasi-elastic, respectively. Near the anticrossings, the quasi-elastic and quasi-magnetic dispersion curves bend away from each other and switch roles. Thus, a wave with energy primarily concentrated in elastic oscillations transfers that energy into magnetic waves when the frequency is through an anticrossing, while the corresponding magnetic wave transfers its energy into elastic vibrations. Two examples of anticrossings are shown in Fig. 2, one at lower frequency and one at higher frequency.

More generally, uncoupled magnetic dispersion curves (36) are approximately parabolic, while uncoupled elastic curves (35) are approximately linear. These curves

have two intersections, so there are two regimes at which magnetoelastic interactions occur. The first intersection often occurs in the single or tens of gigahertz regime, where dipole effects are comparable or stronger than exchange. Due to the longer wavelengths, these interactions can often be studied in finite-thickness samples analytically using a thin film assumption [9]. These lower-frequency interactions have been studied experimentally; see, for example [6, 18, 21–23, 37, 81, 82]. The second dispersion curve intersection occurs in a much higher frequency regime, where exchange effects dominate. In this work, we will focus on the higher-frequency interactions, which are not as well-studied but are important for understanding the recovery of magnetic order post ultrafast demagnetization [20].

Even when layering is incorporated, we still expect to see magnetoelastic interactions in the ω - k region near where the bulk shear and magnetic dispersion curves intersect, i.e. $\omega_{\text{m}} \approx \omega_{\text{el}}$. For YIG and Ni, the higher-frequency intersections between the shear elastic and magnetic waves are around 100-200 GHz, and so are well within the current experimentally accessible regime. The longitudinal speeds of sound are twice as large (see Tab. I). Consequently, longitudinal-magnetic waves are expected to occur at twice the frequency range. The separation of A_1 and A_2 from the other wave components in the bulk limit indicates that the most significant elastic-magnetic interactions will involve the A_3 shear elastic component and m_1, m_2 .

We also note that the higher-frequency magnetic and elastic intersections in Fig. 2 for Ni occur at wavelengths $2\pi/k \approx 15$ nm. This is approximately twice the exchange length ℓ for nickel (see Tab. I). Consequently, we expect the exchange energy to be more significant than the long-range dipole energy. Nevertheless, dipole effects must still be considered. A similar argument holds for YIG which has an exchange length $\ell \approx 17$ nm, and its magnetoelastic intersections occur at a similar wavelength.

In summary, analysis of the bulk dispersion curves reveals that magnetoelastic anticrossings between magnetic and shear waves are possible in the extremely high frequency regimes of experimental interest and exchange effects will be more significant than long-range dipole effects in this regime.

B. Single layer asymptotic calculation

When finite-thickness and boundary effects are included, a direct analytical calculation of the dispersion from the eigenvalue problem (28), (32) is challenging. In contrast to the bulk limit, a finite-thickness film in the continuum approximation has an infinite number of dispersion curves, corresponding to higher-order quasi-elastic and quasi-magnetic modes. Of course, the actual number is limited by the crystal lattice spacing. In this section, we utilize an asymptotic calculation that is presented in Appendix A to show that, unlike in the bulk

limit, not all magnetic-elastic curve intersections yield anticrossing behavior.

Motivated by the analysis in the previous subsection, we consider a simplified scenario where displacements in the A_1 and A_2 direction are ignored. We also neglect dipole effects, i.e., we set $g \equiv 0$. These assumptions greatly simplify the eigenvalue problem (28) and (32), yet they reveal significant insight into the problem. The uncoupled case ($B_2 = 0$) gives rise to the discrete, infinite family of elastic $\omega_{\text{el},n}$ and magnetic $\omega_{\text{m},j}$ dispersion branches

$$\omega_{\text{el},n} = \sqrt{(c_S k)^2 + (c_L \xi_n)^2}, \quad n = 0, 1, \dots \quad (39a)$$

$$\omega_{\text{m},j} = \omega_{\text{H}} - \omega_{\text{M}} + \beta(k^2 + \xi_j^2), \quad j = 0, 1, \dots, \quad (39b)$$

where $\xi_n = n\pi/d$ is the discrete vertical wavenumber. The corresponding vertical mode profiles are cosines

$$A_{3,n}(x_3) = a_{\text{el},n} \cos(\xi_n x_3), \quad n = 0, 1, \dots, \quad (40a)$$

$$m_{2,j}(x_3) = a_{\text{m},j} \cos(\xi_j x_3), \quad j = 0, 1, \dots \quad (40b)$$

Magnetic materials exhibit weak magnetoelastic coupling B_2 . We find in App. A that this can be quantified by the smallness of the nondimensional parameter

$$\epsilon = B_2 \frac{\gamma^\ell}{c_S} \sqrt{\frac{\mu_0}{\rho}} \ll 1. \quad (41)$$

For example, $\epsilon \approx 0.02$ for both YIG and Ni. An expansion of the frequencies and mode profiles around (39) and (40) for small ϵ determines the following resonance condition

$$\omega_{\text{el},n}(k) \approx \omega_{\text{m},j}(k), \quad n = j, \quad (42)$$

necessary for magnetoelastic frequency corrections that are proportional to ϵ . Otherwise, for nonresonant conditions, the frequency corrections are significantly smaller (proportional to ϵ^2). Equation (42) represents two resonance requirements: i) the wavenumber k must be close to k_* , an intersection of the uncoupled elastic and magnetic dispersion curves, ii) the mode numbers for the elastic and magnetic waves must be the same $n = j$. The frequency corrections are provided in App. A (see eqs. (A18), (A22)) and describe an anticrossing.

Additionally, the resonance condition (42) leads to a wavenumber dependent relative scaling between the elastic and $a_{\text{el},n}$ and magnetic $a_{\text{m},n}$ mode amplitudes (see eq. (A23)). Combining this scaling and the frequency corrections enables one to describe how the frequency transitions from a quasi-elastic or quasi-magnetic branch to the other. The evaluation of the frequency corrections at the point of intersection (k_*, ω_*)

$$\omega_* = \omega_{\text{el},n}(k_*) = \omega_{\text{m},n}(k_*) \quad (43)$$

of the uncoupled dispersion branches (39) determines the anticrossing frequency gap width

$$\Delta_{\text{gap}} = \epsilon \frac{c_S^2 k_*}{\sqrt{\beta \omega_*}}. \quad (44)$$

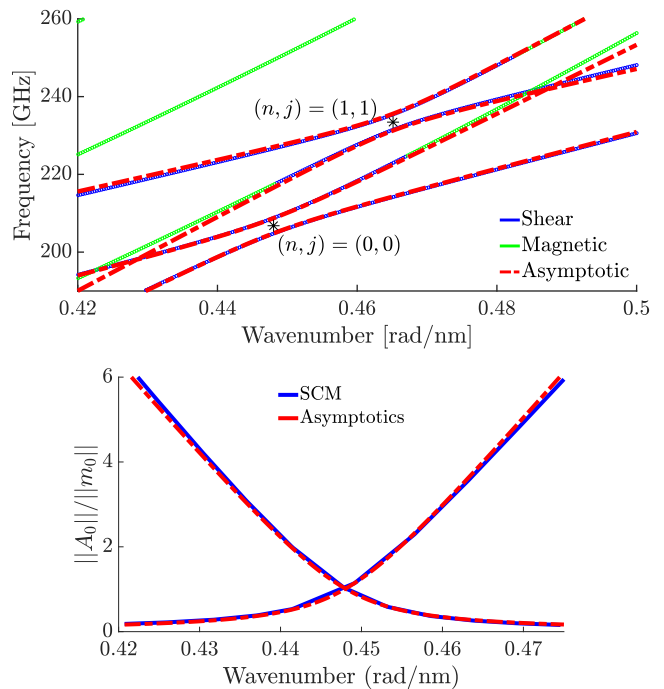


FIG. 3. Top: comparison of the asymptotic prediction (A22) and (A18) (dashed-dotted) with dispersion curves calculated by SCM (solid) for the two lowest modes $n = 0, 1$ and $j = 0, 1$. The material thickness is $d = 30$ nm, and the applied field is $\mu_0 H_0 = 0.2$ T. Intersection points are labeled. Bottom: relative wave magnitudes for the $(n, j) = (0, 0)$ resonant intersection shown on the left plot as determined from numerics (solid) and asymptotics in (A23) (dashed-dotted).

The gap width is proportional to B_2 , as in the bulk and thin film limits [9, 11]. In addition, the gap width is proportional to the wavenumber k_* and inversely proportional to the square root of the frequency ω_* at the intersection (43). Consequently, larger wavenumber and smaller frequency resonances give rise to larger anticrossing gaps.

We compare asymptotic results with the SCM computation, described in the next Section, of the simplified system considered here analytically (eq. (A1) with elastic components A_1 , A_2 and dipole field g neglected) for a single layer of YIG. The top panel of Fig. 3 shows that, in the vicinity of $n = 0, 1$ resonant interactions, the agreement between the asymptotic prediction (dash-dotted) and the SCM calculated dispersion curves (solid) is excellent.

On the bottom panel of Fig. 3, we show the relative magnitudes of the nondimensionalized elastic and magnetic waves for the $(n, j) = (0, 0)$ intersection depicted in the top panel. The numerical calculations (solid) for the norm ratio agrees very well with the asymptotic predictions (dash-dotted).

V. SPECTRAL COLLOCATION METHOD

The previous section demonstrated a marked increase in dispersion complexity due to the incorporation of boundary effects for a single, finite-thickness magnetoelastic layer. In this Section, we introduce a spectral collocation method (SCM) for determining the dispersion relations of multiple layers. Unlike the above asymptotic calculation, this method studies the full system (32), including the dipole field (28).

A. Method overview

The SCM approach we develop is adapted from one utilized for purely elastic waves [25, 26, 53]. Consider N points $x^{(j)}$ on the domain $[-1, 1]$ given by the formula

$$x^{(j)} = \cos \frac{(j-1)\pi}{N-1}, \quad j = 1, \dots, N. \quad (45)$$

These are known as Chebyshev points (or Gauss-Chebyshev-Lobatto points) [54]. They arise as the roots of the N^{th} degree Chebyshev polynomial. Their distribution over $[-1, 1]$ is nonuniform and concentrated near the endpoints of the interval. More details about Chebyshev points and Chebyshev polynomial interpolation can be found in [54, 83].

For each layer, the six functions $A_1(x_3)$, $A_2(x_3)$, $A_3(x_3)$, $m_1(x_3)$, $m_2(x_3)$, and the dipole field $g(x_3)$ are interpolated at Chebyshev points (45) into vectors of length N ,

$$\mathbf{A}_1 = [A_1(x^{(1)}) \dots A_1(x^{(N)})]^T, \dots \quad (46)$$

The key to the efficiency of the SCM method is that, for smooth functions, a discretization at Chebyshev nodes (45) converges faster than any negative power of N , i.e. the convergence is spectral. In fact, one can show that the Chebyshev points are nearly optimal for minimizing the uniform norm of the interpolation error [54].

Each derivative with respect to x_3 of the discretized functions can be approximated using a Chebyshev differentiation matrix D_N . These matrices can be efficiently and stably generated using the *cheb* function in MATLAB [54]. The differentiation matrix D_N generated using the MATLAB function *cheb* must be scaled by $2/(b-a)$ to account for a general domain $[a, b]$. Concatenating the matrices and vectors \mathbf{A}_1, \dots , yields a quadratic polynomial eigenvalue problem of the form $(\mathcal{A}_2\omega^2 + \mathcal{A}_1\omega + \mathcal{A}_0)\phi = 0$, where A_j , $j = 0, 1, 2$ are dense $6N \times 6N$ matrices for a single magnetic layer.

Next, the boundary conditions are incorporated by replacing the rows representing the boundaries for each of the vector equations. The boundary rows occur at rows $1, N, N+1, 2N, \dots, 6N$ and are discretized with Chebyshev differentiation matrices as above. Then these equations are inserted into the $1, N, N+1, 2N, \dots, 6N$ rows of the polynomial eigenvalue problem. Since our boundary

conditions are time-independent and therefore frequency independent, the boundary effects are all incorporated into \mathcal{A}_0 , and the corresponding $1, N, N+1, \dots$ rows of \mathcal{A}_2 and \mathcal{A}_1 are replaced with zeros.

Polynomial eigenvalue problems can be solved directly using the built-in MATLAB *polyeig* command. The frequency polynomial is second degree, so in principle we will find $12N$ modes for a coupled magnetoelastic layer. An increase in N leads to an increase in the number of approximated eigenvalues, with new, larger eigenvalues appearing while the smaller eigenvalues exhibit improved accuracy. Due to spectral convergence, N need not be very high before accurate results are obtained for the smaller eigenvalues.

In the polynomial eigenvalue problem, the linear in ω terms arise from the Landau-Lifshitz equation (23), which is a first order in time system of differential equations. The quadratic ω^2 terms arise from the Navier equation (16), which is second order in time. Previous spectral collocation methods applied to purely elastic problems (e.g. [25]) only required the solution of an eigenvalue problem for ω^2 , not a polynomial eigenvalue problem, since the square root and splitting into two \pm branches can be computed afterward.

The extension of the above method to multiple layers is straightforward. We outline it for a magnetoelastic material layered on a purely elastic substrate. The substrate has three governing equations for the displacements \bar{A}_j , $j = 1, 2, 3$ (we denote displacements in the substrate by an overbar), for a total of nine equations. The discretized field matrix for these equations ($3N \times 3N$) is joined to the discretized field matrix above to form a matrix with $(9N)^2$ elements. The differentiation matrix in each layer D_N must be suitably scaled to account for the thicknesses of the two layers. Once again, the appropriate boundary conditions replace rows $1, N, N+1, \dots, 9N$. The larger quadratic eigenvalue problem is solved to obtain the solution.

The generated matrices in the polynomial eigenvalue problem can be ill-conditioned, so the problem is numerically sensitive. In order to ensure sufficient numerical precision, we utilize a multi-precision MATLAB toolbox to perform calculations in quadruple precision. Higher precisions than quadruple did not appear to increase the accuracy, and the toolbox is calibrated to perform optimally in quadruple precision [84]. Moreover, we found that many of our calculations yield similarly accurate results even for double precision computations.

One advantage of the SCM method is the direct computation of the dipole field g . Accounting for dipole effects is one of the most significant challenges when studying magnetic waves. By including g as a discretized function in the polynomial eigenvalue problem, we spectrally converge to the correct dipole field with little additional computational cost.

Another benefit of the SCM method is that the eigenvector determined from the polynomial eigenvalue problem is a composite vector containing the discretized ver-

tical mode profiles $\mathbf{A}_1, \mathbf{A}_2, \dots, \mathbf{m}_1, \dots$ at the Chebyshev points (45). We utilize this fact for two purposes. First, we can compare the relative 2-norms of these vectors to classify the mode type corresponding to a particular dispersion curve. For example, if $\|\mathbf{A}_1\| \gg \|\mathbf{A}_2\|$, the displacement is predominately in the x_1 -direction, and the wave can be considered longitudinal. Using the scaling between magnetism and elasticity determined from the nondimensionalization (A2), we can compare $\|\mathbf{A}_i\|/A_*$ and $\|\mathbf{m}_j\|/M_s$ to determine whether a mode is predominately elastic or magnetic. Due to the polarization of magnetic waves, all calculations involving the vectors \mathbf{m}_1 and \mathbf{m}_2 instead utilize the 2-norm of the magnetization vector, $\mathbf{m} = \sqrt{|\mathbf{m}_1|^2 + |\mathbf{m}_2|^2}$. In the below figures displaying results of the SCM method, each dispersion curve is labeled by color to identify the eigenvector's component that is largest, with the appropriate scalings given by (A2). This classification method is simple, and the below figures will indicate its effectiveness.

The discretized eigenvector can be used to determine the vertical mode profile by using the Chebyshev interpolating polynomial corresponding to the discretization. To ensure the property (34), we first apply a complex phase shift so that the vertical shear profile evaluated at the top of the upper layer is positive $A_3(d) > 0$. Then, we present the real parts of A_2, A_3 , and m_2 together and, separately, the $\pi/2$ out of phase imaginary parts of A_1 and m_1 . In order to compare profiles of elastic and magnetic components, they are first nondimensionalized according to (cf. eq. (A2b))

$$A_i/A_*, \quad i = 1, 2, 3, \quad m_j/M_s, \quad j = 1, 2,$$

and then normalized by the maximum amplitude. Wave profiles are presented below in Figs. 5, 9, and 10.

A validation study is performed in Appendix B. We observe rapid convergence of the frequencies requiring only a modest number of Chebyshev discretization points $N \in \{10, \dots, 24\}$. Furthermore, we directly compare the uncoupled $B_2 = 0$ elastic dispersion computed using SCM for a double layer with a published elastic dispersion solver, finding quantitative agreement.

VI. RESULTS

In this section, we review some selected results of SCM calculations in order to highlight its utility. In all figures in this section, curves with mode profiles whose 2-norms are dominated by magnetism are green, elastic waves in a magnetic material are blue, and elastic waves in a nonmagnetic material are red. In addition, variables corresponding to a nonmagnetic material are denoted by a bar, e.g., \bar{A}_1 .

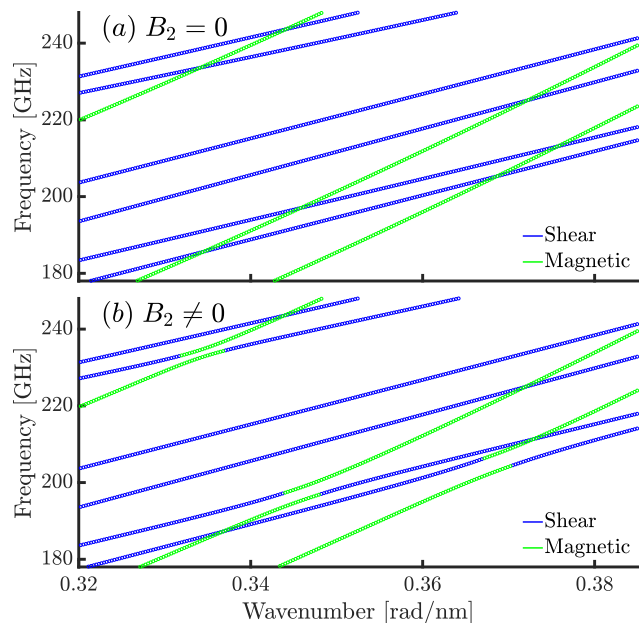


FIG. 4. Dispersion curves for one layer of YIG with thickness 30 nm and $N = 16$ with coupling constant $B_2 = 0$ for (a) and the physical value of B_2 in Tab. I for (b). Three anticrossings and multiple ordinary crossings are visible.

A. Single layer

1. Dispersion map

We first examine the effect of magnetoelastic coupling on a single layer. Figure 4 shows SCM calculations with $N = 16$ for a single layer of YIG with thickness 30 nm and an applied field of 0.25 T. Panel (a) shows the uncoupled result when $B_2 = 0$, resulting in purely elastic or magnetic modes. The dispersion curves cross without any interaction.

In contrast, panel (b) has a nonzero coupling constant B_2 set to the physical value for YIG given in Tab. I. Away from the intersections, the dispersion curves are nearly identical between panels (a) and (b). Near some intersections, however, anticrossings appear, as expected. Multiple simple crossings are also displayed. One can readily observe that the anticrossing gap width decreases with increasing frequency and lower wavenumber. These findings are consistent with the simplified analysis presented in Sec. IV.

2. Resonant and nonresonant interactions

We next examine resonant and nonresonant interactions in the single layer of YIG. In the top panel of Fig. 5, we show a zoomed in view of the two lowest-order anticrossings from Fig. 4(b). The wave profiles at the labeled points are shown in the bottom panels. For the purposes of resonances and comparing the number of zeros, we

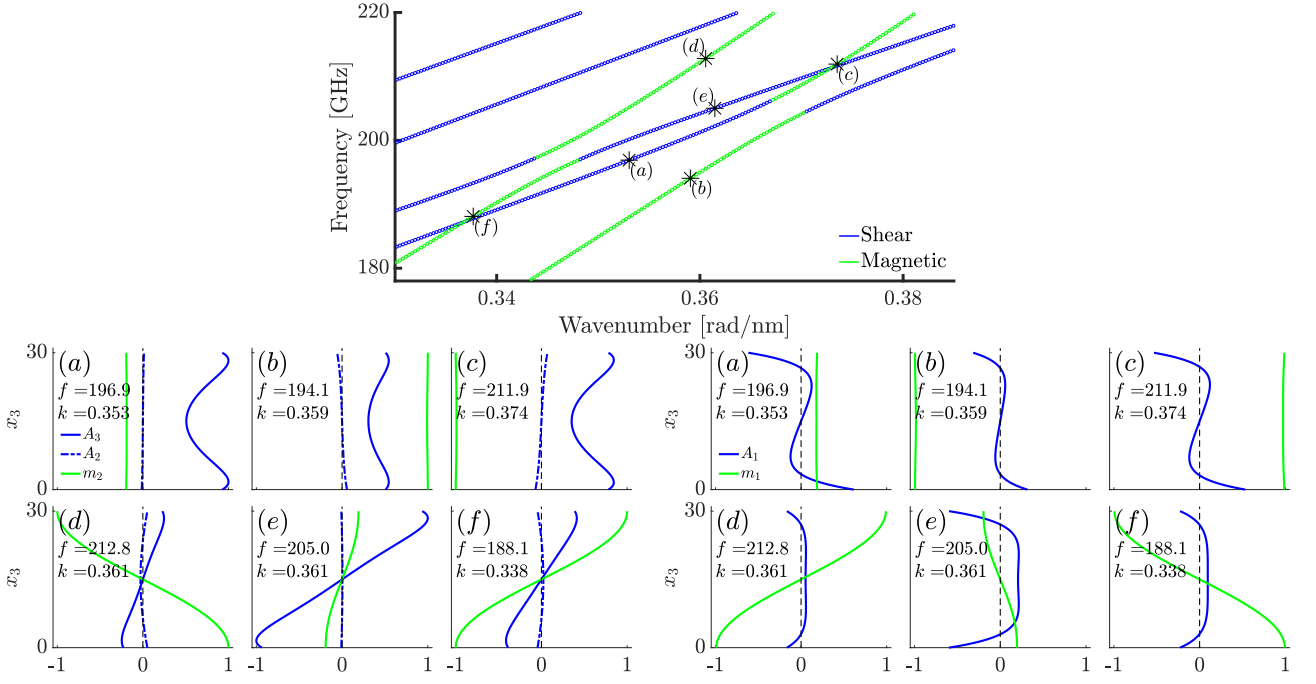


FIG. 5. Top: zoomed in anticrossings from Fig. 4(b). Bottom: mode profiles corresponding to the dispersion points (a)–(f) with (A_3, A_2, m_2) (Left) and the $\pi/2$ phase advanced profiles (A_1, m_1) (Right). Points (a) – (c) correspond to an anticrossing in the zeroth order mode of A_3 and (m_1, m_2) , so the wave profiles do not exhibit zeros. Points (d) – (f) correspond to the first order mode in A_3 and (m_1, m_2) , so their profiles have a single zero. Figures (c) and (f) are the profiles at nonresonant crossings; the nonresonant correction is higher order and not visible in this figure.

focus on the dominant modal contributions from vertical shear A_3 and magnetism (m_1, m_2) . Notice the general similarity between the resonant magnetic and elastic modes in each row of Fig. 5, Left. Points (a) – (c) correspond to an anticrossing in the zeroth order mode, so the wave profiles A_3, m_2 do not exhibit zeros, i.e., they are resonant. Points (d) – (f) correspond to a different anticrossing originating from first order modes, so their profiles have a single zero. When the dispersion curves from these two separate anticrossings intersect each other, an additional anticrossing does not occur because the mode numbers differ. Figures (c) and (f) are the magnetic profiles at nonresonant crossings; the nonresonant correction is very small and not visible in this figure.

Although the asymptotic calculation in section IV B made several simplifying assumptions, its main findings are qualitatively verified. For exchange-dominated waves, anticrossings only appear between resonant magnetic and elastic modes. In addition, Fig. 5 clearly shows that the higher-order anticrossings decrease in their gap width. This is consistent with (A22), which predicts that the gap width will decrease with increasing frequency and decreasing wave number. Finally, close observation reveals that the quasi-magnetic and quasi-elastic dispersion curves in Fig. 5 are slightly shifted from their uncoupled locations.

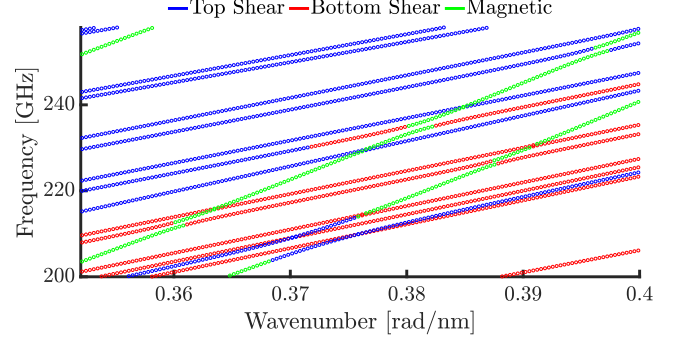


FIG. 6. Dispersion curves for one layer of YIG with thickness 30 nm and $N = 12$ layered on a 50 nm film of GGG. Numerous anticrossings are visible.

B. Two layers

1. Dispersion map

Next, we incorporate a second, nonmagnetic layer and examine its effect on the magnetoelastic dispersion curves. Figure 6 shows the dispersion map for 30 nm of YIG layered on a 50 nm substrate of GGG. The plot axes were chosen to show a large number of anticrossings. Elastic shear waves localized in the YIG layer are colored blue, while shear waves localized in the GGG layer are

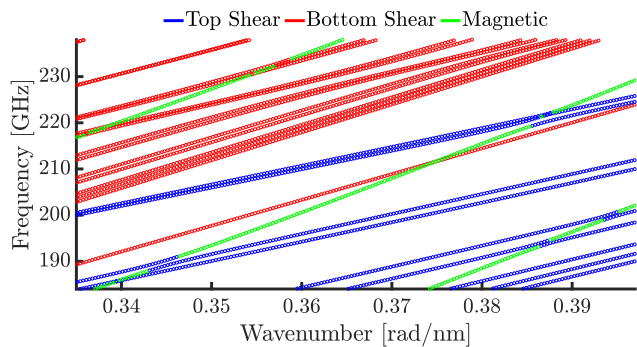


FIG. 7. Dispersion curves for one layer of Ni with thickness 50 nm and $N = 12$ layered on a 100 nm film of Si_2N_3 (right).

red. Magnetic waves are green. Note that there are significantly more dispersion curves here than in Fig. 4, indicating that adding a second layer significantly increases the dispersion complexity.

Interestingly, the magnetic dispersion curves interact with elastic modes from each layer, even though the bottom layer is nonmagnetic. In other words, an elastic wave with energy localized in the nonmagnetic substrate can still interact resonantly with a magnetic-dominated mode. One consequence of this observation is that a single dispersion curve can transition between a quasi-elastic wave in the top layer to a quasi-elastic wave in the bottom layer or a quasi-magnetic wave, depending on the wavenumber and frequency regime.

In Fig. 7, we show a dispersion map for a different sample consisting of 50 nm of Ni layered on a 100 nm Si_2N_3 substrate. One essential difference between this calculation and that of Fig. 6 is that here, the shear speed c_S of the bottom material is larger than that of the top material. This is visible in the large number of dispersion modes with energy localized in the bottom material (red curves) located at higher frequencies than the modes with energy localized in the top material (blue curves).

Similar effects are seen here as in Fig. 6. Modes with energy primarily in the nonmagnetic substrate can still interact with magnetic modes, resulting in a single dispersion branch that transitions between all three wave types. We examine this phenomenon in more detail next.

2. Multimode dispersion branch in a double layer

Now, we continuously follow a single dispersion curve in a YIG-GGG layered material to understand how energy can transition from magnetic to elastic or vice-versa as well as between layers. The top panel of Fig. 8 shows a zoomed-in view of a portion of Fig. 6. Dispersion curves with energy primarily located in the A_2 and \bar{A}_2 modes have been removed for ease of visualization since they play no role in the resonance discussed here.

One dispersion curve in Fig. 8 has been highlighted

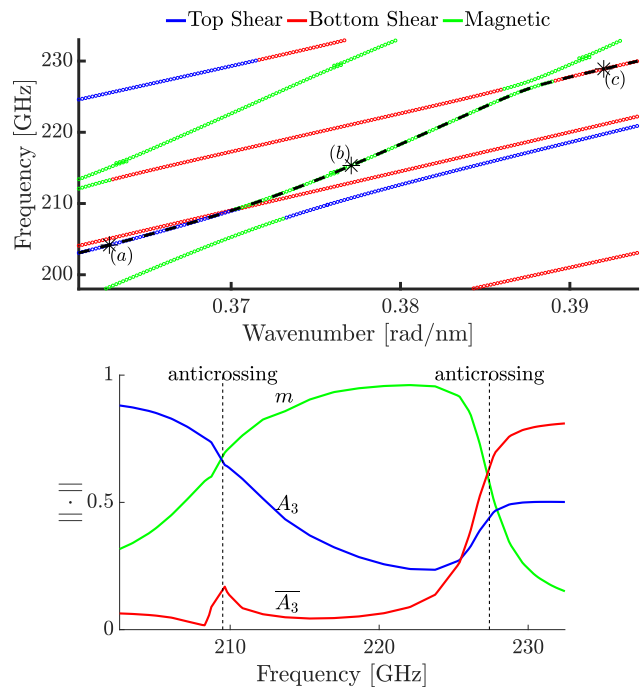


FIG. 8. Top: dispersion curves for 30 nm film of YIG layered on 50 nm of GGG with $N = 24$. Bottom: relative magnitudes of the A_3 , \bar{A}_3 , and m modes for the dispersion curve indicated by a dashed line in the top figure.

using a black dashed line. This curve begins as a quasi-elastic wave localized in the top elastic layer. After an anticrossing it becomes quasi-magnetic, and then after a second anticrossing it becomes quasi-elastic, localized in the bottom layer. This transition is shown more clearly in the bottom panel of Fig. 8, which depicts the relative magnitudes of the three primary wave elements as the frequency is increased.

We further examine the three points labeled (a), (b), and (c) in Fig. 9. The top panel in Fig. 9 shows a bar graph with the relative 2-norms of all seven mode components, suitably scaled according to (A2), for the three points. From this figure, it is clear that the energy in point (a) is primarily localized in the A_3 elastic component of the magnetic layer, in point (b) it is in the magnetic components (m_1, m_2), and in point (c) it is in \bar{A}_3 , the elastic component of the nonmagnetic substrate.

Finally, the vertical mode profiles at the three labeled points are shown in the bottom panel of 9. At points (a) and (b), the elastic portion of the wave is localized primarily at the top surface of the magnetic layer, adjacent to vacuum. However, when the mode becomes dominated by vertical shear elastic oscillations in the nonmagnetic layer, the mode is excited across much of the nonmagnetic layer. This is accompanied by a vertical shear component with about half the energy in the magnetic layer and a small magnetic excitation.

Interestingly, the mode profiles for anticrossings in a

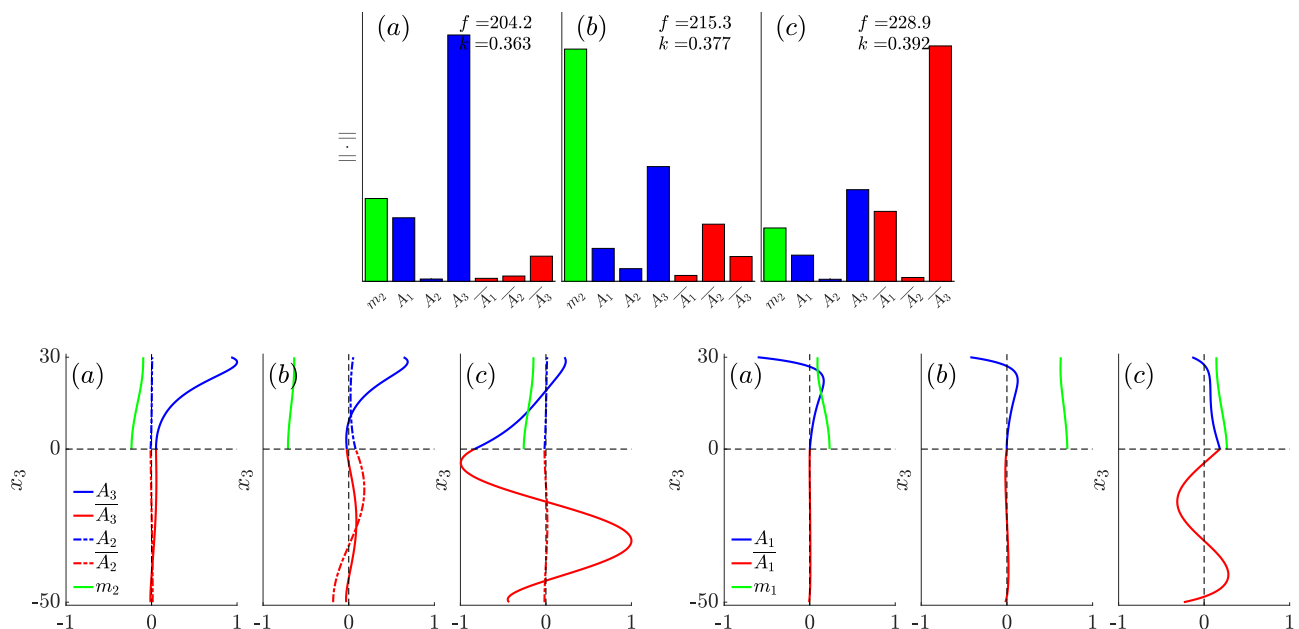


FIG. 9. Top: Relative 2-norms of the scaled displacements and magnetic modes for the points labeled in Fig. 8. Bottom: corresponding wave profiles of the $(A_3, \bar{A}_3, A_2, \bar{A}_2, m_2)$ components (Left) and the $\pi/2$ phase advanced (A_1, \bar{A}_1, m_1) components (Right), calculated with $N = 32$. The dominant contributions are: (a) a vertically sheared surface acoustic wave A_3 , (b) a spin wave (m_1, m_2) , and (c) an oscillatory bulk substrate mode \bar{A}_3 .

layered material do not display as simple of a resonance behavior as for a single layer (see Fig. 5). For example, the magnetic mode profile in Fig. 9 is order 0, the top material elastic mode is order 0 or 1, and the bottom material elastic mode is order 1 or 2. This causes an asymmetry with respect to the layer center in the magnetic waves. In contrast, this asymmetry is not observed in single layers nor in the low frequency calculations of the next section. This indicates that, for a layered material, resonant and nonresonant interactions have added complexity which is not captured by our simplified asymptotic calculation. Nevertheless, the presence of some anticrossings and some simple crossings is consistent with our analytical findings.

To summarize, the highlighted dispersion curve in Fig. 8 and corresponding figures in this section reveal that for increasing frequency, magnetism acts as a mediator to transfer energy between a surface shear wave in the magnetic material to a shear wave across the non-magnetic substrate.

C. Low frequency interactions

For completeness, we also present some dispersion and wave profile results for waves in a lower-frequency range, shown in Fig. 10. The main phenomenological difference for this 1–4 GHz regime is that dipole effects are much stronger relative to exchange effects. Thus, our exchange-dominated asymptotic calculation is not presumed to be

valid here. To ensure the presence of multiple dispersion modes, we increase the material thicknesses to $0.2 \mu\text{m}$ of YIG layered on $0.3 \mu\text{m}$ of GGG.

Figure 10 shows two quasi-elastic modes and three quasi-magnetic modes in the dispersion map with four resonant anticrossings and two nonresonant crossings visible. One interesting observation from the wave profiles is that the order zero (panels (b) and (e)) magnetic mode appears to track the middle quasi-magnetic dispersion curve, with higher frequency than the first order magnetic mode in panel (d).

The leftmost quasi-elastic dispersion curve (panel (a)) appears to be a transverse shear, zeroth-order elastic mode with energy concentrated in A_2 , while the rightmost quasi-elastic curve (panels (d), (e), (f)) is also a zeroth-order mode but with energy concentrated in vertical shear A_3 . The A_2 mode only has an anticrossing with the second magnetic mode, which from panels (b) and (e) also appears to be a zeroth-order mode. This is generally consistent with the asymptotic results obtained earlier regarding resonant and nonresonant anticrossings.

However, the A_3 mode (panels (d), (e), and (f)) displays anticrossing behavior with all three magnetic modes. Apparently, the presence of strong dipole effects alters whether magnetoelastic intersections are resonant or nonresonant. Since the dipole effects occur in the vertical x_3 -direction, this may explain why resonant and nonresonant interactions are still present for the A_2 -mode, which does not experience as strongly the presence of the dipole effective field.

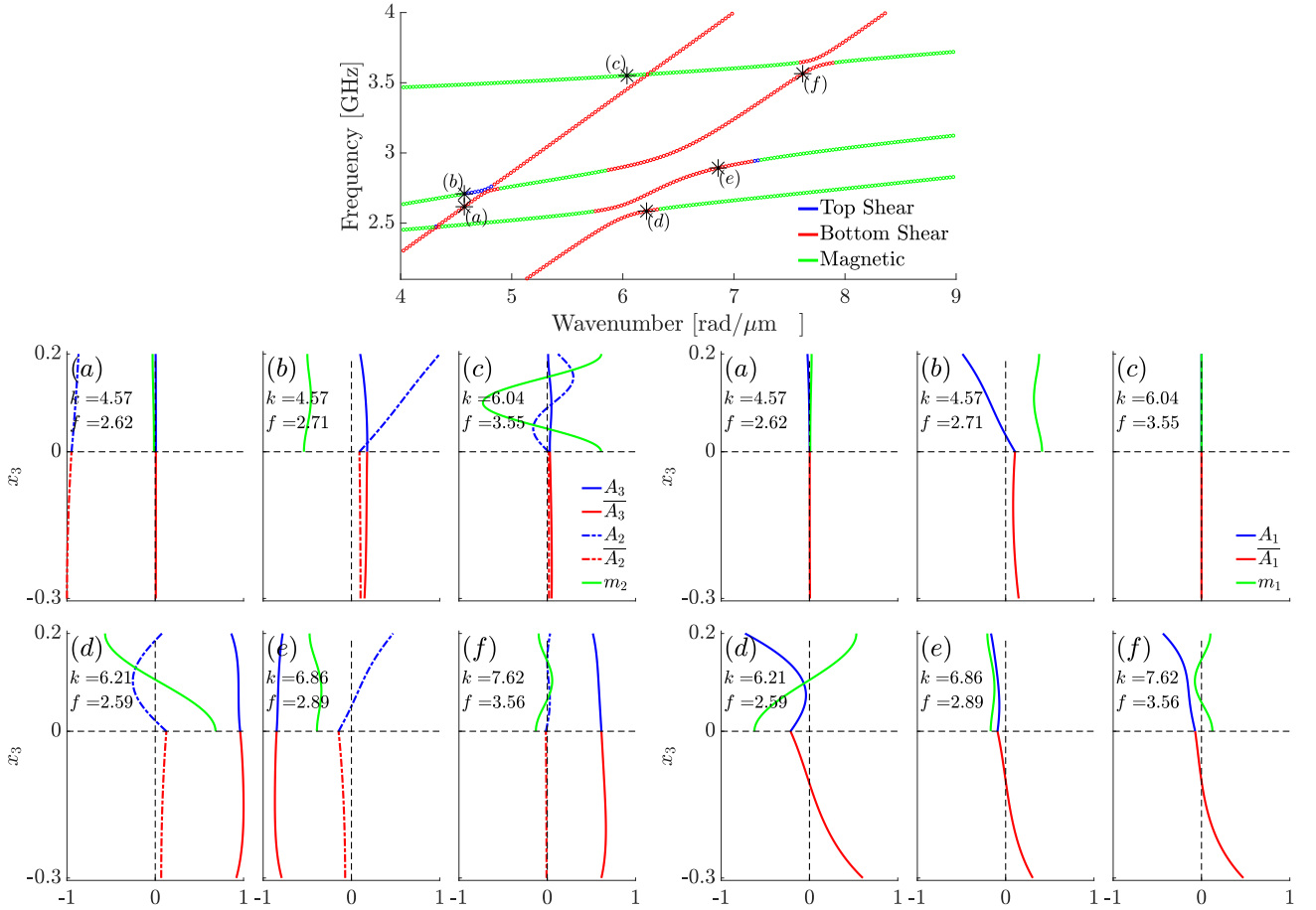


FIG. 10. Top: dispersion map for $0.2 \mu\text{m}$ of YIG layered on $0.3 \mu\text{m}$ of GGG with $N = 16$. Multiple anticrossings and nonresonant crossings are visible. Bottom: wave profiles for the labeled points in the top figure. Resonant and nonresonant interactions are more complicated. For this figure, all wavenumbers are in $\text{rad}/\mu\text{m}$.

VII. DISCUSSION AND CONCLUSION

The main contribution of this work is an analysis of magnetoelastic dispersion in finitely thick and layered materials. We first presented fully coupled magnetoelastic equations, which were then linearized to obtain a coupled system of ordinary differential equations in the vertical, layered direction. This system was analyzed analytically and numerically.

Analytically, we performed an asymptotic calculation to study multiple dispersion curve crossings and anticrossings in a single layer. We identified that anticrossings only occur when the uncoupled magnetic and elastic dispersion curves are resonant with each other. These anticrossings were well-modeled using asymptotic predictions. We also correctly predicted a small but noticeable correction for nonresonant dispersion curve intersections from the uncoupled case. Despite performing our calculations on a simplified scenario, these same general behaviors were observed numerically for the full equations in a single layer. The calculation assumed weak magneto-

elastic coupling, which is the case for all known materials.

Numerically, we introduced a magnetoelastic spectral collocation method (SCM), a fast, simple, accurate, direct approach for calculating the dispersion curves of a magnetoelastic, layered material. Discretizing the coupled system of differential equations at Chebyshev points yields a polynomial eigenvalue problem whose solutions are the angular frequencies for a given wavenumber. Solving this polynomial eigenvalue problem for a mesh of wavenumbers gives both dispersion curves and corresponding wave profiles.

The speed and reliability of SCM was first validated in multiple ways. We then applied SCM to a variety of materials and samples. First, we calculated the dispersion curves for a 30 nm layer of YIG surrounded by a vacuum. This dispersion map revealed a number of anticrossings and simple crossings. Examining the corresponding wave structures supported our analytical result that, for a single layer, anticrossings only occur for resonant magnetic and elastic waves.

Next, we calculated dispersion curves for two differ-

ent double layers. Both calculations showed complex dispersion maps with numerous anticrossings. In addition, it was observed that the same dispersion curve can transition between quasi-elastic in the top layer, quasi-magnetic, and then quasi-elastic in the bottom, nonmagnetic layer. The magnetic curve is resonant with an elastic curve in both the bottom and top layers, and so mediates energy transfer between them with increasing frequency. This curve was subsequently investigated by examining the wave structures at various points.

We also found that resonant and nonresonant interactions are significantly complicated by dipole effects and layering. Both effects can lead to results that are at odds with our simplified analytical predictions for a single layer and negligible dipole field. This highlights the importance of the numerical method for determining the solutions to the full linearized system of differential equations.

We emphasize the fact that SCM is easily generalizable to many magnetoelastic wave applications. The method works just as effectively for GHz frequency ranges as for the extremely high frequency ranges primarily considered here. Calculations for a material with an in-plane magnetic field are also readily obtainable. In that case, the linearization assumptions would lead to a slightly different set of differential equations, but these can be similarly discretized and converted into a polynomial eigenvalue problem. The implementation is straightforward, and spectral convergence ensures fast computational times. In addition, SCM is also applicable to more complex anisotropies and geometries, such as a spherical material or a material with more layers. For example, experimental work reported in [23] studied magnetoelastic waves in a layer of GGG between two layers of YIG. Although the computational complexity would be increased by the need to incorporate dipole-dipole interactions, SCM could be adapted to this scenario to provide valu-

able insights.

Another advantage of SCM is the ability to recover wave profiles with spectral accuracy. These profiles can then be utilized to classify the dispersion mode type. In addition, we can identify transitions along a dispersion curve between the various wave types. This ability to recover wave profiles could also lead in some interesting directions. Ultrafast magnetism experiments measuring scattering intensities using an XFEL yield only a wavenumber-frequency relation; they contain no information about the wave type or structure. By fitting experimentally-obtained dispersion curves to SCM results, one can predict information about the wave structure. Similarly, wave structure data can also aid in the calculation of surface waves such as Rayleigh or Love modes, or waves localized to an interface, another area with many practical applications.

ACKNOWLEDGMENTS

The work of SR and MAH was partially supported by the U.S. Department of Energy, Office of Science, Grant No. DE-SC0018237. The authors are grateful to Thomas J. Silva for suggesting this problem and many inspiring discussions. SR also thanks Danny Ramasawmy for helpful communication in the development of this method.

Appendix A: Asymptotic calculation of exchange-dominated magnetoelastic dispersion

Setting A_1 , A_2 , and g to zero in the eigenvalue problem (32) leaves three equations for m_1 , m_2 , and A_3 . These can be further simplified by solving (32d) for m_1 in terms of m_2 , differentiating twice, and inserting into (32e) so that m_1 is eliminated. If we write $m \equiv m_2$ and $A \equiv A_3$ for convenience, then the new, simplified eigenvalue problem is sixth order

$$(\omega^2 - c_S^2 k^2)A + c_L^2 A'' - \frac{kB_2}{\omega \rho M_s} [(\omega_H - \omega_M + \beta k^2)m - \beta m''] = 0, \quad (\text{A1a})$$

$$[\omega^2 - (\omega_H - \omega_M + \beta k^2)^2]m + 2\beta(\omega_H - \omega_M + \beta k^2)m'' - \beta^2 m'''' - \omega k \gamma B_2 A = 0, \quad (\text{A1b})$$

for $0 < x_3 < d$. Recall the definitions of ω_H , ω_M and β in (37). The corresponding six boundary conditions are

$$A' \equiv m' \equiv m''' \equiv 0, \quad x_3 = 0, \quad x_3 = d. \quad (\text{A1c})$$

It will be helpful to nondimensionalize (A1). For this, we introduce the scalings

$$\begin{aligned} \tilde{k} &= k/K, & \tilde{\omega} &= \omega/\Omega, & \tilde{x}_3 &= Kx_3, \\ \tilde{m} &= m/M_s, & \tilde{A} &= A/A_*, \end{aligned} \quad (\text{A2a})$$

where all nondimensional quantities are distinguished

from their dimensional counterpart by a tilde $\tilde{\cdot}$. Furthermore, the wavenumber, frequency, and elastic displacement scalings are

$$K = c_S/\beta, \quad \Omega = c_S K, \quad A_* = \sqrt{\frac{M_s \beta}{\rho c_S^2 \gamma}}. \quad (\text{A2b})$$

The lowest order magnetoelastic intersection occurs for the spatially uniform elastic mode; hence the frequency scaling $\Omega = c_S K$. The wavenumber K is determined by equating elastic and quadratic exchange dispersion

$c_S K = \beta K^2$, determining a natural length scale for the waves in this problem. The magnetization M_s and displacement A_* scalings provide the means to directly compare magnetic and elastic mode amplitudes. This scaling is used in all mode comparison plots: Figs. 5, 8, 9, and 10. The scalings in (A2) imply that $\tilde{\omega} = \tilde{k} = 1$ when the lowest order uncoupled dispersion branches intersect $\omega_H = \omega_M$. Under the above scalings, we obtain the nondimensional applied field parameter \tilde{H} and elasticity constant \tilde{G} ,

$$\tilde{H} = \frac{(\omega_H - \omega_M)\beta}{c_S^2}, \quad \tilde{G} = \frac{c_L}{c_S}. \quad (\text{A2c})$$

Finally, we introduce the nondimensional magnetoelastic coupling parameter ϵ in eq. (41). Then, upon using (41) and (A2), the eigenvalue problem (A1) becomes

$$(\tilde{\omega}^2 - \tilde{k}^2)\tilde{A} + \tilde{G}^2\tilde{A}'' - \epsilon\frac{\tilde{k}}{\tilde{\omega}}[(\tilde{H} + \tilde{k}^2)\tilde{m} - \tilde{m}'] = 0, \quad (\text{A3a})$$

$$[\tilde{\omega}^2 - (\tilde{H} + \tilde{k}^2)^2]\tilde{m} + 2(\tilde{H} + \tilde{k}^2)\tilde{m}'' - \tilde{m}'''' - \epsilon\tilde{\omega}\tilde{k}\tilde{A} = 0, \quad (\text{A3b})$$

for $0 < \tilde{x}_3 < \tilde{d} = \frac{c_S d}{\beta}$. For nickel, $\epsilon \approx 0.019$, while for YIG $\epsilon \approx 0.023$, both small parameters (see Table I). The two physical parameters \tilde{H} and \tilde{G} are $\mathcal{O}(1)$, as are $\tilde{\omega}$ and \tilde{k} . Under the above transformation, the boundary conditions become

$$\tilde{A}' \equiv \tilde{m}' \equiv \tilde{m}''' \equiv 0, \quad \tilde{x}_3 = 0, \quad \tilde{x}_3 = \tilde{d}. \quad (\text{A3c})$$

For a layer of nickel with thickness $d = 50$ nm, $\tilde{d} \approx 24 \gg 1$. We now perform an asymptotic analysis of (A3) as $\epsilon \rightarrow 0^+$.

1. Zeroth order solution

First, we consider the uncoupled equations. Setting $\epsilon = 0$ in (A3) yields the mode profiles

$$\tilde{A}_n(\tilde{x}_3) = \tilde{a}_{\text{el},n} \cos(\tilde{\xi}_n \tilde{x}_3), \quad n = 0, 1, \dots, \quad (\text{A4a})$$

$$\tilde{m}_j(\tilde{x}_3) = \tilde{a}_{\text{m},j} \cos(\tilde{\xi}_j \tilde{x}_3), \quad j = 0, 1, \dots, \quad (\text{A4b})$$

with right hand sides

$$\begin{aligned} F_1 &= -\tilde{\omega}_n^{(1)} \tilde{A}_n^{(0)} [3(\tilde{\omega}_n^{(0)})^2 - \tilde{k}^2 - \tilde{G}^2 \tilde{\xi}_n^2], \\ G_1 &= \tilde{k} \tilde{\omega}_n^{(0)} \tilde{A}_n^{(0)}. \end{aligned} \quad (\text{A8})$$

where $\tilde{\xi}_n = n\pi/\tilde{d}$ is the vertical wavenumber. The uncoupled dispersion relations for these modes are

$$\tilde{\omega}_n(\tilde{k}) = \sqrt{\tilde{k}^2 + \tilde{G}^2 \tilde{\xi}_n^2}, \quad n = 0, 1, 2, \dots, \quad (\text{A5a})$$

$$\tilde{\omega}_j(\tilde{k}) = \tilde{H} + \tilde{k}^2 + \tilde{\xi}_j^2, \quad j = 0, 1, 2, \dots \quad (\text{A5b})$$

Note that there are actually two dispersion branches for each component $\pm\tilde{\omega}$, but we will focus on the two positive branches in (A5a), (A5b). These are the dispersion curves for a single layer. As $\tilde{d} \rightarrow \infty$, the dispersion curves converge to the bulk dispersion curves in which $\tilde{\xi}_n, \tilde{\xi}_j \rightarrow 0$.

2. Quasi-elastic and quasi-magnetic waves

Next, we consider the effect of coupling on quasi-elastic and quasi-magnetic dispersion. We expand around the uncoupled modes (A4) and dispersion branches (A5) using the weak coupling parameter ϵ . First, we expand around a purely elastic wave, assuming a weak magnetic component

$$\begin{aligned} \tilde{\omega} &\sim \tilde{\omega}_n^{(0)} + \epsilon \tilde{\omega}_n^{(1)} + \epsilon^2 \tilde{\omega}_n^{(2)}, \\ \tilde{A}_n(\tilde{x}_3) &\sim \tilde{A}_n^{(0)}(\tilde{x}_3) + \epsilon \tilde{A}_n^{(1)}(\tilde{x}_3) + \epsilon^2 \tilde{A}_n^{(2)}(\tilde{x}_3), \\ x \tilde{m}_n(\tilde{x}_3) &\sim \epsilon \tilde{m}_n^{(1)}(\tilde{x}_3) + \epsilon^2 \tilde{m}_n^{(2)}(\tilde{x}_3), \end{aligned} \quad (\text{A6})$$

for $0 < \epsilon \ll 1$. The zeroth order mode $\tilde{A}_n^{(0)}$ corresponds to the profile in (A4a), while $\tilde{\omega}_n^{(0)}$ corresponds to the uncoupled elastic dispersion frequency branch of order n (A5a). Then, at $\mathcal{O}(\epsilon)$, eq. (A3) becomes

$$\tilde{\omega}_n^{(0)} [(\tilde{\omega}_n^{(0)})^2 - \tilde{k}^2] \tilde{A}_n^{(1)} + \tilde{\omega}_n^{(0)} \tilde{G}^2 (\tilde{A}_n^{(1)})'' = F_1, \quad (\text{A7a})$$

$$[(\tilde{\omega}_n^{(0)})^2 - (\tilde{H} + \tilde{k}^2)^2] \tilde{m}_n^{(1)} + 2(\tilde{H} + \tilde{k}^2) (\tilde{m}_n^{(1)})'' - (\tilde{m}_n^{(1)})'''' = G_1, \quad (\text{A7b})$$

The orthogonality (solvability) condition for $\tilde{A}_n^{(1)}(\tilde{x}_3)$ in (A7a) (see, e.g., [85]) implies that $\tilde{\omega}_n^{(1)} = 0$. Thus, (A7a) is a homogeneous equation, and the particular solution

is $\tilde{A}_n^{(1)} \equiv 0$. We can solve (A7b) for $\tilde{m}_n^{(1)}(\tilde{x}_3)$ as

$$\begin{aligned} \tilde{m}_n^{(1)}(\tilde{x}_3) &= \tilde{b}_n \tilde{a}_{\text{el},n} \cos(\tilde{\xi}_n \tilde{x}_3), \\ \tilde{b}_n &= \frac{\tilde{\omega}_n^{(0)} \tilde{k}}{(\tilde{\omega}_n^{(0)})^2 - (\tilde{H} + \tilde{k}^2)^2 - 2\tilde{\xi}_n^2(\tilde{H} + \tilde{k}^2) - \tilde{\xi}_n^4}. \end{aligned} \quad (\text{A9})$$

Importantly, the solution (A9) only holds when the asymptotic expansion (A6) remains well-ordered, i.e., \tilde{b}_n is at most $\mathcal{O}(1)$. Consequently, when the denominator of \tilde{b}_n is small

$$(\tilde{\omega}_n^{(0)})^2 - (\tilde{H} + \tilde{k}^2)^2 - 2\tilde{\xi}_n^2(\tilde{H} + \tilde{k}^2) - \tilde{\xi}_n^4 \leq \mathcal{O}(\epsilon), \quad (\text{A10})$$

we obtain the precise statement of the resonance condition (42). In this case, we require an alternative asymptotic expansion. Equation (A10) is satisfied when the elastic curve of order n (A5a) intersects a magnetic dispersion curve of the same order $j = n$ (A5b). Thus, the asymptotic expansion (A6) is only valid far from these resonant interactions. It is not valid when magnetic and elastic dispersion curves are in resonance, a case which we describe below.

In order to determine the higher-order frequency correction $\tilde{\omega}_n^{(2)}$, we continue on to $\mathcal{O}(\epsilon^2)$, which yields the same equations as in (A7) but with $\tilde{A}_n^{(1)} \rightarrow \tilde{A}_n^{(2)}$, $\tilde{m}_n^{(1)} \rightarrow \tilde{m}_n^{(2)}$ and the alternative right hand sides

$$\begin{aligned} F_2 &= \tilde{k}[(\tilde{H} + \tilde{k}^2)\tilde{m}_j^{(1)} - (\tilde{m}_j^{(1)})''] - 2\tilde{A}_n^{(0)}(\tilde{\omega}_n^{(0)})^2\tilde{\omega}_n^{(2)}, \\ G_2 &= \tilde{k}\tilde{\omega}_n^{(0)}\tilde{A}_n^{(1)}. \end{aligned} \quad (\text{A11})$$

Since the elastic correction $\tilde{A}_n^{(1)}(\tilde{x}_3) \equiv 0$, we obtain $\tilde{m}_j^{(2)}(\tilde{x}_3) = 0$. After inserting the solution for $\tilde{m}_j^{(1)}(\tilde{x}_3)$ in (A9) into (A11) and requiring solvability for $\tilde{A}_n^{(2)}$, we obtain the second order dispersion curve correction

$$\tilde{\omega}_n^{(2)} = \frac{B_n}{2(\tilde{\omega}_n^{(0)})^2}(\tilde{H} + \tilde{k}^2 + \tilde{\xi}_n^2). \quad (\text{A12})$$

Thus, a quasi-elastic dispersion curve, away from resonant intersections with a magnetic dispersion curve, has the $\mathcal{O}(\epsilon)$ magnetic component (A9), and the $\mathcal{O}(\epsilon^2)$ shift in frequency (A12).

We can similarly expand around a quasi-magnetic dispersion curve as

$$\begin{aligned} \tilde{\omega} &\sim \tilde{\omega}_j^{(0)} + \epsilon\tilde{\omega}_j^{(1)} + \epsilon^2\tilde{\omega}_j^{(2)}, \\ \tilde{A}_j(\tilde{x}_3) &\sim \epsilon\tilde{A}_j^{(1)}(\tilde{x}_3) + \epsilon^2\tilde{A}_j^{(2)}(\tilde{x}_3), \\ \tilde{m}_j(\tilde{x}_3) &\sim \tilde{m}_j^{(0)}(\tilde{x}_3) + \epsilon\tilde{m}_j^{(1)}(\tilde{x}_3) + \epsilon^2\tilde{m}_j^{(2)}(\tilde{x}_3). \end{aligned} \quad (\text{A13})$$

Here, the zeroth order solution $\tilde{m}_j^{(0)}(\tilde{x}_3)$ corresponds to (A4b), while $\tilde{\omega}_j^{(0)}$ corresponds to (A5b). A similar calculation to the quasi-elastic case yields $\tilde{\omega}_j^{(1)} = 0$, $\tilde{m}_j^{(1)} = 0$,

and

$$\begin{aligned} \tilde{A}_j^{(1)}(\tilde{x}_3) &= C_j \tilde{m}_j \cos(\tilde{\xi}_j \tilde{x}_3), \\ C_j &= \frac{\tilde{k}}{\tilde{\omega}_j^{(0)}[(\tilde{\omega}_j^{(0)})^2 - \tilde{k}^2 - \tilde{G}^2\tilde{\xi}_j^2]}, \end{aligned} \quad (\text{A14})$$

as long as the resonance condition

$$(\tilde{\omega}_j^{(0)})^2 - \tilde{k}^2 - \tilde{G}^2\tilde{\xi}_j^2 \leq \mathcal{O}(\epsilon) \quad (\text{A15})$$

is not met. Note that (A15) is identical to (A10) when $n = j$. A similar solvability condition at $\mathcal{O}(\epsilon^2)$ yields the higher-order correction in the quasi-magnetic frequency,

$$\tilde{\omega}_j^{(2)} = \frac{\tilde{k}C_j}{2}. \quad (\text{A16})$$

We compare the approximate dispersion curve predictions (A12) and (A16) with results from the SCM code for the system (A1) in the top panel of Fig. A1. Due to the higher order correction calculated above, the actual intersection of the dispersion curves is not equal to the intersection of the dispersion curves in the absence of coupling. The asymptotic prediction of this new intersection also shows excellent agreement with the SCM calculations.

We also compare the wave profiles from SCM with the asymptotic predictions (A9) and (A14) in the bottom panel of Fig. A1. The asymptotic predictions show excellent agreement with numerical calculations.

3. Resonant interactions

Next, we examine the interactions near intersections of elastic and magnetic dispersion curves, i.e. when the conditions (A10) and (A15) are met. We denote uncoupled dispersion intersection points as $(\tilde{k}_*, \tilde{\omega}_*)$, which are given by $\tilde{\omega}_* = \tilde{\omega}_j(\tilde{k}_*) = \tilde{\omega}_n(\tilde{k}_*)$ for some j, n in (A5), with \tilde{k}_* the corresponding wave number. From (A5a) and (A5b), we have

$$\tilde{k}_*^2 = -\tilde{H} + \frac{1}{2} - \tilde{\xi}_j^2 + \frac{1}{2}\sqrt{1 + 4(\tilde{G}^2\tilde{\xi}_n^2 - \tilde{\xi}_j^2 - \tilde{H})}, \quad (\text{A17a})$$

$$\tilde{\omega}_*^2 = \tilde{k}_*^2 + \tilde{G}^2\tilde{\xi}_n^2 = (\tilde{H} + \tilde{k}_*^2 + \tilde{\xi}_j^2)^2, \quad (\text{A17b})$$

where we have made a sign choice for \tilde{k}_*^2 in order to have real solutions for \tilde{k}_* . We expand around the intersection point $(\tilde{k}_*, \tilde{\omega}_*)$ for $0 < \epsilon \ll 1$ as

$$\begin{aligned} \tilde{k} &\sim \tilde{k}_* + \epsilon\Delta, & \tilde{A}_n(\tilde{x}_3) &\sim \tilde{A}_n^{(0)}(\tilde{x}_3) + \epsilon\tilde{A}_n^{(1)}(\tilde{x}_3), \\ \tilde{\omega} &\sim \tilde{\omega}_* + \epsilon f(\Delta), & \tilde{m}_j(\tilde{x}_3) &\sim \tilde{m}_j^{(0)}(\tilde{x}_3) + \epsilon\tilde{m}_j^{(1)}(\tilde{x}_3). \end{aligned} \quad (\text{A18})$$

One key difference from the previous expansions (A6) and (A13) is that an expansion for the wavenumber \tilde{k}

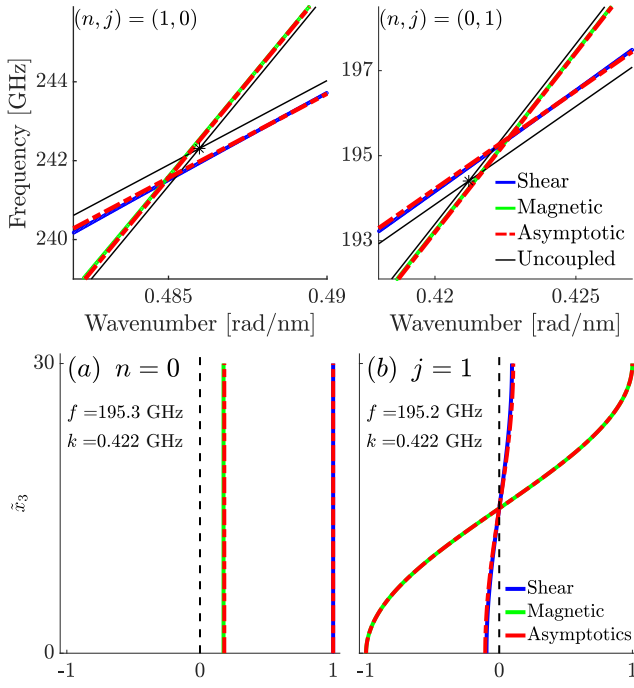


FIG. A1. Top: two figures comparing the dimensional asymptotic prediction (dash-dotted) with results from the SCM method (solid). The uncoupled dispersion (solid) is also plotted to show that the coupled dispersion curves differ slightly. Bottom: comparison of the asymptotic predictions (dash-dotted) (A9) and (A14) with normalized, nondimensionalized wave profiles from SCM (solid) for two dispersion curves. (a) A quasi-elastic wave with $n = 0$ and an $\mathcal{O}(\epsilon)$ magnetic component. (b) A quasi-magnetic wave with $j = 1$ and an $\mathcal{O}(\epsilon)$ elastic component.

is also included, i.e., we are only considering the dispersion in a neighborhood of the intersection point $(\tilde{k}_*, \tilde{\omega}_*)$. The variables Δ and $f(\Delta)$ represent small changes in the wavenumber and frequency, respectively. The zeroth order solutions $\tilde{m}_j^{(0)}$ and $\tilde{A}_n^{(0)}$ again correspond to the solutions found above in (A4) but they are now both included in the leading order asymptotic expansion (A18).

At $\mathcal{O}(\epsilon)$, upon simplification using the relationships between $\tilde{\omega}_*$ and \tilde{k}_* given in (A17) as well as (A4), the system (A3) becomes

$$(\tilde{\omega}_*^2 - \tilde{k}_*^2)\tilde{A}_n^{(1)} + \tilde{\omega}_*\tilde{G}^2(\tilde{A}_n^{(1)})'' = \tilde{k}_*\tilde{m}_j^{(0)} + \tilde{A}_n^{(0)}[2\tilde{k}_*\Delta - 2\tilde{\omega}_*f], \quad (\text{A19a})$$

$$(\tilde{\omega}_*^2 - (\tilde{H} + \tilde{k}_*^2))\tilde{m}_j^{(1)} + 2(\tilde{H} + \tilde{k}_*^2)(\tilde{m}_j^{(1)})'' - (\tilde{m}_j^{(1)})'''' = (4\tilde{k}_*\tilde{\omega}_*\Delta - 2\tilde{\omega}_*f)\tilde{m}_j^{(0)} + \tilde{\omega}_*\tilde{k}_*\tilde{A}_n^{(0)}. \quad (\text{A19b})$$

In order for the above system (A19) to be solvable, we require that the right hand side be orthogonal to $[\cos(\tilde{\xi}_n\tilde{x}_3), \cos(\tilde{\xi}_j\tilde{x}_3)]^T$, i.e., the following inner products hold

$$\int_0^{\tilde{d}} [\tilde{k}_*\tilde{a}_{m,j} \cos(\tilde{\xi}_j\tilde{x}_3) + (2\tilde{k}_*\Delta - 2\tilde{\omega}_*f)\tilde{a}_{el,n} \cos(\tilde{\xi}_n\tilde{x}_3)] \cos(\tilde{\xi}_n\tilde{x}_3) d\tilde{x}_3 = 0, \quad (\text{A20a})$$

$$\int_0^{\tilde{d}} [(4\tilde{k}_*\tilde{\omega}_*\Delta - 2\tilde{\omega}_*f)\tilde{a}_{m,j} \cos(\tilde{\xi}_j\tilde{x}_3) + \tilde{\omega}_*\tilde{k}_*\tilde{a}_{el,n} \cos(\tilde{\xi}_n\tilde{x}_3)] \cos(\tilde{\xi}_j\tilde{x}_3) d\tilde{x}_3 = 0. \quad (\text{A20b})$$

The intersections of resonant modes occur where $n = j$ in (A20). Then the above integrals imply

$$\begin{bmatrix} \tilde{k}_* & 2(\tilde{k}_*\Delta - \tilde{\omega}_*f) \\ 4\tilde{k}_*\Delta - 2f & \tilde{k}_* \end{bmatrix} \begin{bmatrix} \tilde{a}_{m,n} \\ \tilde{a}_{el,n} \end{bmatrix} = 0. \quad (\text{A21})$$

In order to have a nonzero solution for the coefficients

$\tilde{a}_{m,n}$ and $\tilde{a}_{el,n}$, the matrix in (A21) must be singular. Thus, the determinant must equal zero, yielding two relationships between the change in wavenumber Δ and

frequency f ,

$$f_{\pm}(\Delta) = \frac{\tilde{k}_*}{2\tilde{\omega}_*} \left(\Delta + 2\Delta\tilde{\omega}_* \pm \sqrt{\Delta^2(2\tilde{\omega}_* - 1)^2 + \tilde{\omega}_*} \right). \quad (\text{A22})$$

The two branches of f_{\pm} in (A22) correspond to the two branches of the anticrossing.

The corresponding null space of the singular matrix yields the relative sizes of $\tilde{a}_{m,n}$ and $\tilde{a}_{el,n}$

$$\left(\Delta - 2\Delta\tilde{\omega}_* \mp \sqrt{\Delta^2(2\tilde{\omega}_* - 1)^2 + \tilde{\omega}_*} \right) \tilde{a}_{el,n} = \tilde{a}_{m,n}. \quad (\text{A23})$$

Analyzing (A23) reveals that for f_+ , as $\Delta \rightarrow -\infty$, the magnitude of the elastic displacement $\tilde{a}_{el,n}$ grows large in comparison to magnetism $\tilde{a}_{m,n}$. As $\Delta \rightarrow +\infty$, $\tilde{a}_{m,n}$ grows large in comparison to $\tilde{a}_{el,n}$. These behaviors are reversed for f_- . This implies that the top anticrossing curve transitions from quasi-elastic to quasi-magnetic, while the bottom curve transitions from quasi-magnetic to quasi-elastic. A plot comparing the predicted quasi-elastic and quasi-magnetic dispersion curves with the SCM applied to eqs. (A1) is provided in Fig. 3.

Since $f(0) = \pm \frac{\tilde{k}_*}{2\sqrt{\tilde{\omega}_*}}$, the anticrossing frequency gap has width $\epsilon\tilde{k}_*/\sqrt{\tilde{\omega}_*}$. The dimensional frequency gap is eq. (44). This implies that for anticrossings in a layered material, the gap width depends not only on the coupling strength but also on which intersection is considered in (A17). For anticrossings at lower wavenumbers and higher frequencies, the gap width is predicted to be smaller.

For nonresonant interactions, i.e. when $n \neq j$, then the integral of $\cos(\tilde{\xi}_n\tilde{x}_3)\cos(\tilde{\xi}_j\tilde{x}_3)$ in (A20) is zero. What remains is the following system of equations

$$\tilde{k}_*\Delta - \tilde{\omega}_*f = 0, \quad 4\tilde{k}_*\Delta - 2f = 0. \quad (\text{A24})$$

The system of equations (A24) is solved either by $\Delta = f = 0$ or $\tilde{\omega}_* = 1/2$. The second of these solutions is not generic. The first solution implies that higher order effects are necessary, as there is no interaction at $\mathcal{O}(\epsilon)$. This is consistent with the earlier finding that, away from anticrossings, i.e., for nonresonant interactions, magnetoelastic coupling only has a $\mathcal{O}(\epsilon^2)$ effect on the dispersion curves.

To summarize, in this Appendix, we showed that finite thickness effects lead to an infinite number of dispersion curves in a material. The many intersections between magnetic and elastic curves can be classified as resonant or nonresonant, depending on whether the quasi-elastic and quasi-magnetic waves share the same order. For exchange-dominated waves, only resonant interactions yield anticrossings. Nonresonant interactions only display simple crossings, which nevertheless experience an $\mathcal{O}(\epsilon^2)$ shift from their uncoupled intersections.

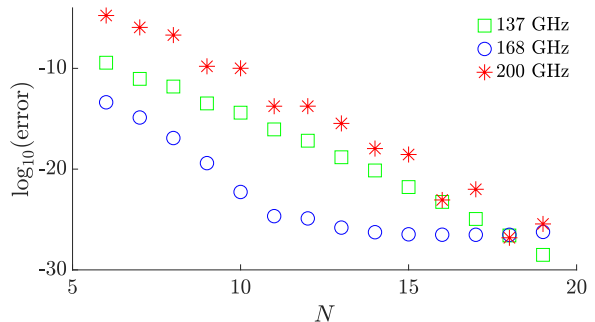


FIG. A2. Convergence of frequency values for $k = 0.3$ rad/nm on a logarithmic scale. The material studied is 30 nm of YIG on 50 nm of GGG. Each data point shows the relative error with the frequency value calculated for $N = 20$. Due to calculations performed in quadruple precision, convergence is to 10^{-30} , after which rounding errors dominate.

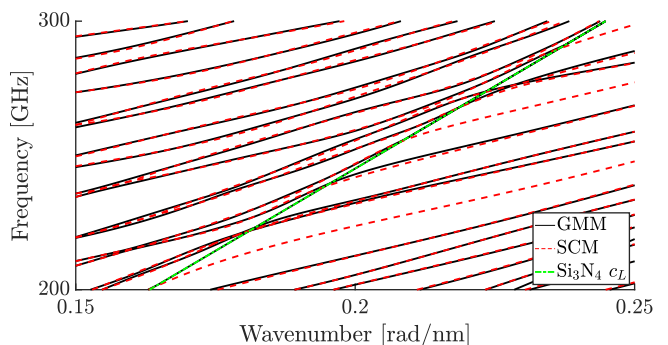


FIG. A3. Comparison between SCM (dashed) and GMM (solid) methods in the absence of magnetism for 50 nm of Ni layered on 100 nm of Si_3N_4 with $N = 24$. GMM incorrectly identifies the Si_3N_4 longitudinal speed of sound c_L as a dispersion curve, and other GMM dispersion curves remain trapped in this incorrect minimum.

Appendix B: Validation of SCM

In order to validate the SCM approach, we examine the convergence of eigenvalues (i.e. frequencies) as the discretization N is increased. In Fig. A2, we show the convergence of three frequency values for $k = 0.3$ rad/nm corresponding to three types of waves for the YIG-GGG double layer. The three frequency values were calculated for each value of N for $6 < N < 20$, and then the relative error with the frequency calculated at $N = 20$ is displayed on a log scale. Even for higher frequencies, the convergence is rapid and the errors are small.

As another validation step, we compare SCM results to GMM results from a published solver, namely the ElasticMatrix MATLAB toolbox [27]. ElasticMatrix computes dispersion curves in a layered, purely elastic material utilizing a GMM approach. Ignoring the magnetic coupling, we calculate elastic dispersion curves for the Ni- Si_3N_4 double layer using our SCM code by zeroing the coupling

coefficient $B_2 = 0$ and compare with the toolbox results.

The results of this comparison for $N = 24$ are presented in Fig. A3. For most all of the dispersion curves, excellent agreement between the SCM and GMM approaches are obtained. It is important to explain the discrepancies. First, the GMM approach incorrectly identifies the silicon nitride longitudinal speed of sound as a dispersion curve (dashed green). This has been previously identified as a shortcoming of GMM calculations [25]. Second, some curves are only found by the SCM approach. We hypothesize that this occurs when the GMM curve-tracing algorithm ends up trapped by the (incorrect) speed of sound dispersion curves. Missed curves have also been previously reported as a shortcoming of the GMM method [25].

We stress that, running on the same machine, the SCM code to generate Fig. A3 had a run time of less than ten minutes. In contrast, the ElasticMatrix method required over ten hours to compute nearly identical dispersion curves.

A third validation for SCM is its close agreement with the asymptotic analysis shown in Sec. IV B. Since the asymptotic calculation included an analytical calculation of the uncoupled magnetic and elastic dispersion curves in a simplified layered material, the agreement in the vicinity of the anticrossing in Fig. 3 validates that the code accurately recovers these curves. Combined with the excellent agreement for nonresonant crossings in Fig. A1, we have ample evidence that the SCM reliably incorporates coupling effects.

-
- [1] O. W. Richardson, A Mechanical Effect Accompanying Magnetization, *Phys. Rev. (Series I)* **26**, 248 (1908).
- [2] S. J. Barnett, On Magnetization by Angular Acceleration, *Science* **30**, 413 (1909).
- [3] A. Einstein and W. de Haas, Experimenteller Nachweis der Ampereschen Molekularströme, *Deutsche Physikalische Gesellschaft, Verhandlungen* **17**, 152 (1915).
- [4] A. Einstein and W. de Haas, Experimental proof of the existence of Ampere's molecular currents, *Koninklijke Akademie van Wetenschappen Te Amsterdam, Proceedings* **18**, 696 (1915).
- [5] S. Barnett, Magnetization by rotation, *Physical Review* **6**, 239 (1915).
- [6] A. Kamra, H. Keshtgar, P. Yan, and G. E. W. Bauer, Coherent elastic excitation of spin waves, *Phys. Rev. B* **91**, 104409 (2015).
- [7] S. Streib, H. Keshtgar, and G. E. W. Bauer, Damping of Magnetization Dynamics by Phonon Pumping, *Phys. Rev. Lett.* **121**, 027202 (2018).
- [8] A. Rückriegel and R. A. Duine, Long-Range Phonon Spin Transport in Ferromagnet–Nonmagnetic Insulator Heterostructures, *Phys. Rev. Lett.* **124**, 117201 (2020).
- [9] F. Vanderveken, J. Mulkers, J. Leliaert, B. Van Waeyenberge, B. Sorée, O. Zografos, F. Ciubotaru, and C. Adelman, Confined magnetoelastic waves in thin waveguides, *Phys. Rev. B* **103**, 054439 (2021).
- [10] C. Kittel, Interaction of spin waves and ultrasonic waves in ferromagnetic crystals, *Phys. Rev.* **110**, 836 (1958).
- [11] A. Gurevich and G. Melkov, *Magnetization Oscillations and Waves* (CRC Press, London, 1996).
- [12] E. Vedmedenko, R. Kawakami, D. Sheka, P. Gambardella, A. Kirilyuk, A. Hirohata, C. Binek, O. Chubykalo-Fesenko, S. Sanvito, B. Kirby, J. Grollier, E.-S. K., T. Kampfrath, C.-Y. You, and A. Berger, The 2020 magnetism roadmap, *J. Phys. D: Appl. Phys* **53**, 453001 (2020).
- [13] A. Barman, G. Gubbiotti, S. Ladak, A. O. Adeyeye, M. Krawczyk, J. Gräfe, C. Adelman, S. Cotozana, A. Naeemi, V. I. Vasyuchka, B. Hillebrands, S. A. Nikitov, H. Yu, D. Grundler, A. V. Sadovnikov, A. A. Grachev, S. E. Sheshukova, J.-Y. Duquesne, M. Marangolo, G. Csaba, W. Porod, V. E. Demidov, S. Urazhdin, S. O. Demokritov, E. Albisetti, D. Petti, R. Bertacco, H. Schultheiss, V. V. Kruglyak, V. D. Poimanov, S. Sahoo, J. Sinha, H. Yang, M. Münzenberg, T. Moriyama, S. Mizukami, P. Landeros, R. A. Gallardo, G. Carlotti, J.-V. Kim, R. L. Stamps, R. E. Camley, B. Rana, Y. Otani, W. Yu, T. Yu, G. E. W. Bauer, C. Back, G. S. Uhrig, O. V. Dobrovolskiy, B. Budinska, H. Qin, S. van Dijken, A. V. Chumak, A. Khitun, D. E. Nikonov, I. A. Young, B. W. Zingsem, and M. Winklhofer, The 2021 Magnonics Roadmap, *J. Phys.: Condens. Matter* **33**, 413001 (2021).
- [14] A. V. Chumak, P. Kabos, M. Wu, C. Abert, C. Adelman, A. O. Adeyeye, J. Åkerman, F. G. Aliev, A. Anane, A. Awad, C. H. Back, A. Barman, G. E. W. Bauer, M. Becherer, E. N. Beginin, V. A. S. V. Bitencourt, Y. M. Blanter, P. Bortolotti, I. Boventer, D. A. Bozhko, S. A. Bunyaev, J. J. Carmiggelt, R. R. Cheenikundil, F. Ciubotaru, S. Cotozana, G. Csaba, O. V. Dobrovolskiy, C. Dubs, M. Elyasi, K. G. Fripp, H. Fulara, I. A. Golovchanskiy, C. Gonzalez-Ballester, P. Graczyk, D. Grundler, P. Gruszecki, G. Gubbiotti, K. Guslienko, A. Haldar, S. Hamdioui, R. Hertel, B. Hillebrands, T. Hioki, A. Houshang, C.-M. Hu, H. Huebl, M. Huth, E. Iacocca, M. B. Jungfleisch, G. N. Kakazei, A. Khitun, R. Khymyn, T. Kikkawa, M. Kläui, O. Klein, J. W. Klos, S. Knauer, S. Koraltan, M. Kostylev, M. Krawczyk, I. N. Krivorotov, V. V. Kruglyak, D. Lachance-Quirion, S. Ladak, R. Lebrun, Y. Li, M. Lindner, R. Macêdo, S. Mayr, G. A. Melkov, S. Mieszczak, Y. Nakamura, H. T. Nembach, A. A. Nikitin, S. A. Nikitov, V. Novosad, J. A. Otálora, Y. Otani, A. Papp, B. Pigeau, P. Pirro, W. Porod, F. Porrati, H. Qin, B. Rana, T. Reimann, F. Riente, O. Romero-Isart, A. Ross, A. V. Sadovnikov, A. R. Safin, E. Saitoh, G. Schmidt, H. Schultheiss, K. Schultheiss, A. A. Serga, S. Sharma, J. M. Shaw, D. Suess, O. Surzhenko, K. Szulc, T. Taniguchi, M. Urbánek, K. Usami, A. B. Ustinov, T. van der Sar, S. van Dijken, V. I. Vasyuchka, R. Verba, S. V. Kusminskiy, Q. Wang, M. Weides, M. Weiler, S. Wintz, S. P. Wolfski, and X. Zhang, Advances in Magnetics Roadmap on Spin-Wave Computing, *IEEE Trans. Magn.* **58**, 1 (2022).
- [15] A. Kirilyuk, A. V. Kimel, and T. Rasing, Ultrafast optical manipulation of magnetic order, *Rev. Mod. Phys.* **82**,

- 2731 (2010).
- [16] J. Walowski and M. Münzenberg, Perspective: Ultrafast magnetism and THz spintronics, *J. Appl. Phys.* **120**, 140901 (2016).
- [17] V. S. Vlasov, A. V. Golov, L. N. Kotov, V. I. Shcheglov, A. M. Lomonosov, and V. V. Temnov, The Modern Problems of Ultrafast Magnetoacoustics (Review), *Acoust. Phys.* **68**, 18 (2022).
- [18] D.-L. Zhang, J. Zhu, T. Qu, D. M. Lattery, R. H. Victora, X. Wang, and J.-P. Wang, High-frequency magnetoacoustic resonance through strain-spin coupling in perpendicular magnetic multilayers, *Sci. Adv.* **6**, eabb4607 (2020).
- [19] A. A. Maznev, R. Mincigrucci, F. Bencivenga, V. Unnikandanunni, F. Capotondi, G. Chen, Z. Ding, R. A. Duncan, L. Foglia, M. G. Izzo, C. Masciovecchio, A. Martinelli, G. Monaco, E. Pedersoli, S. Bonetti, and K. A. Nelson, Generation and detection of 50 GHz surface acoustic waves by extreme ultraviolet pulses, *Appl. Phys. Lett.* **119**, 044102 (2021).
- [20] D. Turenne, A. Yaroslavtsev, X. Wang, V. Unnikandanunni, I. Vaskivskiy, M. Schneider, E. Jal, R. Carley, G. Mercurio, R. Gort, N. Agarwal, B. Van Kuiken, L. Mercadier, J. Schlappa, L. Le Guyader, N. Gerasimova, M. Teichmann, D. Lomidze, A. Castoldi, D. Potorochin, D. Mukkattukavil, J. Brock, N. Zhou Hagström, A. H. Reid, X. Shen, X. J. Wang, P. Maldonado, Y. Kvashnin, K. Carva, J. Wang, Y. K. Takahashi, E. E. Fullerton, S. Eisebitt, P. M. Oppeneer, S. Molodtsov, A. Scherz, S. Bonetti, E. Iacocca, and H. A. Dürr, Nonequilibrium sub-10 nm spin-wave soliton formation in FePt nanoparticles, *Sci. Adv.* **8**, eabn0523 (2022).
- [21] M. Weiler, L. Dreher, C. Heeg, H. Huebl, R. Gross, M. S. Brandt, and S. T. B. Goennenwein, Elastically driven ferromagnetic resonance in nickel thin films, *Phys. Rev. Lett.* **106**, 117601 (2011).
- [22] J. Holanda, D. Major, A. Azevedo, and S. Rezende, Detecting the phonon spin in magnon-phonon conversion experiments, *Nature Phys.* **14**, 500 (2018).
- [23] K. An, A. N. Litvinenko, R. Kohno, A. A. Fuad, V. V. Naletov, L. Vila, U. Ebels, G. de Loubens, H. Hurdquint, N. Beaulieu, J. Ben Youssef, N. Vukadinovic, G. E. W. Bauer, A. N. Slavin, V. S. Tiberkevich, and O. Klein, Coherent long-range transfer of angular momentum between magnon kittel modes by phonons, *Phys. Rev. B* **101**, 060407 (2020).
- [24] M. J. S. Lowe, Matrix techniques for modeling ultrasonic waves in multilayered media, *IEEE Transactions on Ultrasonics, Ferroelectrics, and Frequency Control* **42**, 525 (1995).
- [25] F. Quintanilla, M. Lowe, and R. Craster, Modeling guided elastic waves in generally anisotropic media using a spectral collocation method, *J. of the Acoustical Soc. of Am.* **137**, 1180 (2015).
- [26] F. Quintanilla, Z. Fan, M. Lowe, and R. Craster, Guided waves' dispersion curves in anisotropic viscoelastic single- and multi-layered media, *Proc. R. Soc. A* **471**, 20150268 (2015).
- [27] D. R. Ramasawmy, B. T. Cox, and B. E. Treeby, Elastic-Matrix: A MATLAB toolbox for anisotropic elastic wave propagation in layered media, *Software X* **11**, 100397 (2020).
- [28] R. Becker and W. Döring, *Ferromagnetismus* (Julius Springer, Berlin, 1939).
- [29] C. Kittel, Physical theory of ferromagnetic domains, *Rev. Mod. Phys.* **21**, 541 (1949).
- [30] C. Herring and C. Kittel, On the theory of spin waves in ferromagnetic media, *Phys. Rev.* **81**, 869 (1951).
- [31] E. Schlömann, Generation of phonons in high-power ferromagnetic resonance experiments, *Journal of Applied Physics* **31**, 1647 (1960).
- [32] R. F. Soohoo, General spin-wave dispersion relations, *Phys. Rev.* **120**, 1978 (1960).
- [33] E. R. Callen and H. B. Callen, Static magnetoelastic coupling in cubic crystals, *Phys. Rev.* **129**, 578 (1963).
- [34] R. E. Camley, Magnetoelastic waves in a ferromagnetic film on a nonmagnetic substrate, *Journal of Applied Physics* **50**, 5272 (1979), <https://aip.scitation.org/doi/pdf/10.1063/1.326624>.
- [35] S. Carter, A. Bracker, G. Bryant, M. Kim, M. Zalalutdinov, M. Yakes, C. Czarnocki, J. Casara, M. Scheibner, and D. Gammon, Spin-mechanics coupling of an InAs quantum dot embedded in a mechanical resonator, *Phys. Rev. Lett.* **121**, 246801 (2018).
- [36] S. Whiteley, G. Wolfowicz, C. Anderson, *et al.*, Spin-phonon interactions in silicon carbide addressed by Gaussian acoustics, *Nature Physics* **15**, 490 (2019).
- [37] F. Godejohann, A. V. Scherbakov, S. M. Kukhtaruk, A. N. Poddubny, D. D. Yaremkevich, M. Wang, A. Nadzeyka, D. R. Yakovlev, A. W. Rushforth, A. V. Akimov, and M. Bayer, Magnon polaron formed by selectively coupled coherent magnon and phonon modes of a surface patterned ferromagnet, *Phys. Rev. B* **102**, 144438 (2020).
- [38] M. Matsuo, J. Ieda, and S. Maekawa, Mechanical generation of spin current, *Frontiers in Physics* **3**, 54 (2015).
- [39] A. V. Sadovnikov, A. A. Grachev, A. A. Serdobintsev, S. E. Sheshukova, S. S. Yankin, and S. A. Nikitov, Magnon straintronics to control spin-wave computation: Strain reconfigurable magnonic-crystal directional coupler, *IEEE Magnetism Letters* **10**, 1 (2019).
- [40] R. Verba, V. Tiberkevich, and A. Slavin, Wide-band non-reciprocity of surface acoustic waves induced by magnetoelastic coupling with a synthetic antiferromagnet, *Phys. Rev. Applied* **12**, 054061 (2019).
- [41] Z. Yao, S. Tiwari, T. Lu, J. Rivera, K. Q. T. Luong, R. N. Candler, G. P. Carman, and Y. E. Wang, Modeling of multiple dynamics in the radiation of bulk acoustic wave antennas, *IEEE Journal on Multiscale and Multiphysics Computational Techniques* **5**, 5 (2020).
- [42] E. Fohtung, Magnetostriction fundamentals, in *Reference Module in Materials Science and Materials Engineering* (Elsevier, 2021).
- [43] J. D. N. Cheeke, *Fundamentals and Applications of Ultrasonic Waves*, 2nd ed. (CRC Press, Boca Raton, FL, 2012).
- [44] T. Kundu, *Mechanics of Elastic Waves and Ultrasonic Nondestructive Evaluation* (CRC Press, 2019).
- [45] P. A. Fedders, Theory of acoustic resonance and dispersion in bulk ferromagnets, *Phys. Rev. B* **9**, 3835 (1974).
- [46] M. Wang and G. Wang, 9 - electromagnetic sensors for assessing and monitoring civil infrastructures, in *Sensor Technologies for Civil Infrastructures*, Woodhead Publishing Series in Electronic and Optical Materials, Vol. 55, edited by M. Wang, J. Lynch, and H. Sohn (Woodhead Publishing, 2014) pp. 238–264.
- [47] R. Y. Pak and B. B. Guzina, Three-dimensional Green's functions for a multilayered half-space in displacement

- potentials, *Journal of Engineering Mechanics* **128**, 449 (2002).
- [48] Y. Roganov and A. Stovas, Low-frequency normal wave propagation in a periodically layered medium with weak contrast in elastic properties, *Geophysical Prospecting* **62**, 1205 (2014).
- [49] A. Chattopadhyay, S. Gupta, A. Chattopadhyay, and A. Singh, The dispersion of shear wave in multilayered magnetoelastic self-reinforced media, *International Journal of Solids and Structures* **47**, 1317 (2010).
- [50] R. Verba, I. Lisenkov, I. Krivorotov, V. Tiberkevich, and A. Slavin, Nonreciprocal Surface Acoustic Waves in Multilayers with Magnetoelastic and Interfacial Dzyaloshinskii-Moriya Interactions, *Phys. Rev. Appl.* **9**, 064014 (2018).
- [51] L. Knopoff, A matrix method for elastic wave problems, *Bull. of the Seis. Soc. of Am.* **54**, 431 (1964).
- [52] A. H. Nayfeh, The general problem of elastic wave propagation in multilayered anisotropic media, *The Journal of the Acoustical Society of America* **89**, 1521 (1991).
- [53] A. Adamou and R. Craster, Spectral methods for modelling guided waves in elastic media, *J. of the Acoustical Soc. of Am.* **116**, 1524 (2004).
- [54] L. Trefethen, *Spectral Methods in MATLAB* (Oxford, 2000).
- [55] J. P. Boyd, *Chebyshev and Fourier Spectral Methods* (Dover publications, 2001).
- [56] E. Iacocca, T. Liu, A. Reid, *et al.*, Spin-current-mediated rapid magnon localisation and coalescence after ultrafast optical pumping of ferrimagnetic alloys, *Nature Communications* **10**, 1756 (2019).
- [57] N. Hagström, R. Jangid, D. Meera, *et al.*, Symmetry-dependent ultrafast manipulation of nanoscale magnetic domains, *ArXiv* (2021), <https://arxiv.org/abs/2112.09587>.
- [58] F. Vanderveken, F. Ciubotaru, and C. Adelman, Magnetoelastic Waves in Thin Films, in *Chirality, Magnetism and Magnetoelasticity*, Vol. 138, edited by E. Kamenetskii (Springer International Publishing, Cham, 2021) pp. 287–322.
- [59] H. Kronmüller, General micromagnetic theory and applications, in *Materials Science and Technology* (American Cancer Society, 2019) pp. 1–43.
- [60] L. Landau and E. Lifshitz, *Theory of Elasticity*, 3rd ed., *Course of Theoretical Physics*, Vol. 7 (Elsevier, 1986).
- [61] J. Harris, *Linear Elastic Waves* (Cambridge, 2007).
- [62] C.-Y. Liang, S. M. Keller, A. E. Sepulveda, A. Bur, W.-Y. Sun, K. Wetzlar, and G. P. Carman, Modeling of magnetoelastic nanostructures with a fully coupled mechanical-micromagnetic model, *Nanotechnology* **25**, 435701 (2014).
- [63] W. Strauss, Magnetoelastic properties of yttrium-iron garnet, in *Applications to Quantum and Solid State Physics*, *Physical Acoustics*, Vol. 4, edited by W. P. Mason (Academic Press, 1968) pp. 211–268.
- [64] A. Love, *A Treatise on the Mathematical Theory of Elasticity*, 2nd ed. (Cambridge UP, 1906).
- [65] T. L. Gilbert, A phenomenological theory of damping in ferromagnetic materials, *IEEE Trans. Magn.* **40**, 3443 (2004).
- [66] G. Bertotti, I. Mayergoyz, and C. Serpico, *Nonlinear Magnetization Dynamics in Nanosystems*, Elsevier series in electromagnetism (Elsevier, Oxford, 2009).
- [67] C. Garcia-Cervera, Numerical micromagnetics: a review, *Bol. Soc. Esp. Mat. Apl. SeMA* **39**, 1 (2007).
- [68] D. Stancil and A. Prabhakar, *Spin Waves: Theory and Applications* (Springer, 2009).
- [69] K. Harte, Theory of magnetization ripple in ferromagnetic films, *J. Appl. Phys.* **39**, 1503 (1968).
- [70] K. Neeraj, N. Awari, S. Kovalev, D. Polley, N. Zhou Hagström, S. S. P. K. Arekapudi, A. Semisalova, K. Lenz, B. Green, J.-C. Deinert, I. Ilyakov, M. Chen, M. Bawatna, V. Scalera, M. d'Aquino, C. Serpico, O. Hellwig, J.-E. Wegrowe, M. Gensch, and S. Bonetti, Inertial spin dynamics in ferromagnets, *Nat. Phys.* **17**, 245 (2021).
- [71] E. Olive, Y. Lansac, and J.-E. Wegrowe, Beyond ferromagnetic resonance: The inertial regime of the magnetization, *Appl. Phys. Lett.* **100**, 192407 (2012).
- [72] S. Giordano and P.-M. Déjardin, Derivation of magnetic inertial effects from the classical mechanics of a circular current loop, *Phys. Rev. B* **102**, 214406 (2020).
- [73] J. Rumble, ed., *CRC Handbook of Chemistry and Physics*, 102nd ed. (CRC Press, 2021).
- [74] Silicon Nitride (Si₃N₄) Properties and Applications, <https://www.azom.com/properties.aspx?ArticleID=53>, accessed: 2022-02-21.
- [75] L. Graham and R. Chang, Elastic moduli of single-crystal gadolinium gallium garnet, *J. of Appl. Phys.* **41**, 2247 (1970).
- [76] Z. Tian, D. Sander, and J. Kirschner, Nonlinear magnetoelastic coupling of epitaxial layers of Fe, Co, and Ni on Ir(100), *Phys. Rev. B* **79**, 024432 (2009).
- [77] F. Vanderveken, F. Ciubotaru, and C. Adelman, Magnetoelastic waves in thin films (2020), <https://arxiv.org/abs/2003.12099>, arXiv:2003.12099 [cond-mat.mes-hall].
- [78] M. Wu, Nonlinear spin waves in magnetic film feedback rings, in *Solid State Physics*, Vol. 62, edited by R. E. Camley and R. L. Stamps (Academic Press, Burlington, 2011) pp. 163–224.
- [79] M. A. W. Schoen, J. Lucassen, H. T. Nembach, B. Koopmans, T. J. Silva, C. H. Back, and J. M. Shaw, Magnetic properties in ultrathin 3d transition-metal binary alloys. II. Experimental verification of quantitative theories of damping and spin pumping, *Phys. Rev. B* **95**, 134411 (2017).
- [80] B. A. Kalinikos and A. N. Slavin, Theory of dipole-exchange spin wave spectrum for ferromagnetic films with mixed exchange boundary conditions, *J. Phys. C: Solid State Phys.* **19**, 7013 (1986).
- [81] J.-W. Kim and J.-Y. Bigot, Magnetization precession induced by picosecond acoustic pulses in a freestanding film acting as an acoustic cavity, *Phys. Rev. B* **95**, 144422 (2017).
- [82] J. Janusonis, T. Jansma, Chang, *et al.*, Transient grating spectroscopy in magnetic thin films: Simultaneous detection of elastic and magnetic dynamics, *Scientific Reports* **16**, 29143 (2016).
- [83] J. Mason and D. Handscomb, *Chebyshev polynomials* (Chapman & Hall/CRC, Boca Raton, FL, 2003).
- [84] M. C. T. for MATLAB 4.8.3.14463, (Advanpix LLC., Yokohama, Japan).
- [85] E. J. Hinch, *Perturbation Methods*, Cambridge Texts in Applied Mathematics (Cambridge University Press, Cambridge, 1991).